Journal of Manufacturing Processes 89 (2023) 150–169

Contents lists available at ScienceDirect

Journal of Manufacturing Processes

journal homepage: www.elsevier.com/locate/manpro

A comparative study on drillability of Inconel 625 alloy fabricated by wire arc additive manufacturing

Ferhat Ceritbinmez [a], Ali Günen [b,*], Uğur Gürol [c,d], Gürel Çam [e]

[a] Candy Hoover Group Srl, Eskişehir, Turkiye
[b] Iskenderun Technical University, Faculty of Engineering and Natural Sciences, Department of Metallurgy and Materials Engineering, 31200 Iskenderun-Hatay, Turkiye
[c] Istanbul Gedik University, Faculty of Engineering, Department of Metallurgical & Materials Engineering, Istanbul, Turkiye
[d] Gedik Welding Company, Research, and Development Center, Istanbul, Turkiye
[e] Iskenderun Technical University, Faculty of Engineering and Natural Sciences, Department of Mechanical Engineering, 31200 Iskenderun-Hatay, Turkiye

ARTICLE INFO

Keywords:
Additive manufacturing
Ni-based superalloy
Die-sinking Micro-EDM
Micro-EDM drilling
Orbital drilling
Surface integrity
Kerf

ABSTRACT

In recent years, the cost-effective wire arc additive manufacturing (WAAM) method is increasingly replacing traditional production methods for Ni-based superalloys. However, the effect of high heat input and elemental segregation in the WAAM method on machinability has not yet been adequately investigated. For this purpose, drilling of wrought and WAAM Inconel 625 samples with thermal (i.e., die-sinking micro-EDM and micro-EDM) and mechanical drilling techniques (i.e., orbital and conventional drilling) was investigated in this study. It was observed that thermal drilling methods formed a white layer with a thickness of 20-25 μm and 35-50 μm in the cross-section of wrought and WAAM specimens, respectively, while no white layer was formed in the mechanical methods. The average surface roughness of the inside hole, Ra, obtained in the conventional drilling process has improved by 46.15 %, 94.62 %, and 92.82 %, compared to the orbital, die-sinking, and micro-EDM methods, respectively. Because the drill cutting form and helix angle used in this method facilitated chip evacuation. The best surface roughness was obtained respectively by conventional (0.27–029), orbital (0.51–0.53), die-sinking (4.54–5.88), and micro-EDM drilling (3.54–4.25) methods. In addition, a larger kerf angle is obtained in the WAAM sample compared to the wrought one due to higher residual stress and higher dislocation density in the WAAM alloy. On the other hand, the higher hardness value of WAAM samples provided better surface quality in mechanical drilling methods than wrought material. An increase in surface hardness values up to 25 μm from the surface was detected due to the recast layer formed in thermal drilling methods and the strain hardening occurring on the surface in mechanical drilling methods.

1. Introduction

Superalloys are traditionally produced through casting, forging, and machining processes. However, due to the complex and multiple production steps in the casting and forging processes, the production cycle is often long, and molds are required, which makes the process cost-inefficient [1]. Similarly, machining processes cause significant material waste [2,3], resulting in a much higher production cost of the final product [4,5]. This situation necessitates the production of superalloys, which find extensive applications in advanced engineering fields with innovative alternative methods [3]. Recently, additive manufacturing (AM), defined as an advanced material production method known as 3D printing technology, has provided the potential to create complex shaped components that are difficult to produce with traditional methods. Metal additive manufacturing (MAM) is an innovative alternative manufacturing method that allows complex geometries to be produced by melting metal powders or wires using a focused heat source [6–9]. In this method, a final 3D component with the required size and configuration is created by growing 2D stacks on top of each other layer by layer, based on the design of the computer-aided design (CAD) model. Laser, electron beam, plasma, or electric arc can be used as a heat source in MAM methods [6].

The American Society for Testing and Materials (ASTM) has classified MAM techniques as powder bed fusion, directed energy deposition, binder jetting, and sheet lamination [10,11]. Wire arc additive manufacturing (WAAM), one of the directed energy deposition methods,

* Corresponding author.
E-mail address: ali.gunen@iste.edu.tr (A. Günen).

https://doi.org/10.1016/j.jmapro.2023.01.072
Received 27 November 2022; Received in revised form 26 January 2023; Accepted 26 January 2023

is less complex than established systems, requires lower initial setup costs, has a higher deposition rate, and allows the production of larger parts [12]. In addition, it can provide better energy efficiency than powder-based laser/electron beam-assisted deposition methods [13]. Because of all these, it is generally accepted that it is a more advantageous method [12,13]. It can be seen from the open literature that many alloy groups such as stainless steels [14], titanium alloys [15], aluminum alloys [16], carbon steels, hot tool steels, super alloys [5,6,17] and high entropy alloys [18] have been successfully produced by WAAM.

Ni-based superalloys maintaining their exceptionally high strength and oxidation resistance at relatively high temperatures (up to 980 °C) have made these alloys indispensable in many advanced engineering applications [19]. More than 40 % of the weight of advanced aircraft consists of components made of these alloys [20,21]. The applications of these alloys in aircraft include the main structural parts of aircraft, such as gas turbine components and gas turbine hot-end components [20,22,23]. Among the Ni-based superalloys, Inconel 625 and Inconel 718 alloys are the most common commercially available Ni-based superalloys used in the aerospace industry due to their resistance to harsh environments [24]. However, their machinability is difficult due to their high strength and low thermal conductivity properties. It often results in poor quality in terms of cutting tool life and surface integrity of the workpiece. Therefore, it is crucial for sustainability to improve these alloys' machinability by using a variety of techniques [26].

Karataş and Gökkaya [27] reported that there are approximately one hundred thousand assembly holes in small airplanes and more than one million in large airplanes. Therefore, it is crucial that these alloys used in the aviation industry can be drilled with cost-effective methods without sacrificing their mechanical properties and corrosion resistance. Because the time spent drilling into materials in manufacturing processes constitutes approximately 50–70 % of the entire manufacturing time [28].

Superalloys are considered to be "difficult-to-cut" materials [29]. In the manufacturing industry, machining operations such as milling, turning, and drilling are often the primary methods used to achieve low tolerances on the final part [30]. Due to their poor thermal conductivity, these alloys are subject to adverse thermal effects during conventional machining processes and are, therefore, difficult to drill with conventional machining processes [31]. Thus, non-traditional machining methods such as die sink EDM process, electric discharge machining, ultrasonic machining, etc., are used for the machining of superalloys because these techniques can drill hard alloys with high accuracy and excellent finish, regardless of hardness and melting temperature [31,32]. Furthermore, regardless of the hardness of the materials, successful results are obtained in drilling conductive materials with high mechanical properties by die-sinking micro-EDM, micro-EDM drilling method [31,32]. On the other hand, orbital and conventional drilling methods can be used in cases where dimensional accuracy and surface quality are preferred [33,34].

When the literature is examined, although there are studies on the drillability of superalloys produced by casting and forging methods, it has been seen that there has yet to be a comprehensive study in the literature on the drillability of the superalloys produced by AM methods. For example, Mishra et al. [35] drilled holes in Inconel 625 superalloy using a tubular hollow copper electrode in the Die-Sinking Micro-EDM method. In their study, the effects of processing parameters, such as peak current, pulse-on time, and gap voltage, on material removal rate (MRR), surface roughness (SR), surface crack density (SCD), white layer thickness (WLT), circularity, hole taper, and radial overcut (ROC) were examined. They reported that the increase in peak current causes an increase in hole circularity and hole taper. They also determined that the increase in pulse-on time gives rise to an increase in SR, SCD, circularity, and WLT, while an increase in spark gap voltage increases SR and circularity. In addition, they emphasized that with the TOPSIS integrated Taguchi application approach, the highest MRR (70.32 mm^3/min) and circularity (entry: 0.9842, exit: 0.9631) and the lowest surface roughness (Ra, 5.3 μm), SCD (0.0102 $\mu m/\mu m^2$), WLT (10.25 μm), taper (0.49 deg), and ROC (entry: 0.011 mm, exit: 0.162 mm) were obtained when optimal operating parameters of 15 A current, 300 μs arc duration, and 20 V voltage were used.

Ahmed et al. [36] examined the effect of the use of different electrodes, such as brass (70 % Cu; 30 % Zn), copper (99.9 % Cu), and copper tungsten (25 % Cu; 75 % W), in micro-EDM drilling Inconel 718 alloy, on the MRR, electrode wear rate (EWR) and SR. They reported that the highest MRR was reached when brass electrodes were used, followed by Cu and CuW electrode types. They reported that the CuW electrode exhibited the lowest EWR, followed by brass and copper ones. The copper electrode has higher thermal conductivity (W/mK) and melting point (°C) than the brass electrode, but the copper electrode wears faster due to the higher heating. They emphasized that CuW is the best electrode choice for machining Inconel 718, considering overall performance.

Venkatesan et al. [37] drilled Inconel 625 material with a conventional micro-drilling method using different process parameters such as tool diameter, spindle speed, and feed rate, analyzed hole diameter, circularity, overcut, cylindricity, taper ratio, roundness, MRR characteristics of the holes obtained using Analysis of variance (ANOVA), Taguchi S/N ratio. As a result of the analysis, they reported that the use of high tool diameter reduces circularity error, overcut, taper ratio, hole damage factor, roundness, and hole diameter deviations. However, they also reported that the hole diameter and other output parameters increased when high feed rate and spindle speed parameters were used. As a result of the ANOVA analysis results, they recommended using a larger tool diameter with the lowest spindle speed and feed rate for minimum circularity error, taper ratio, overcut, and hole damage factor.

Attanasio [38] drilled 500 μm diameter holes in AISI 310H stainless steel and Ni-based superalloys, namely Hastelloy C22 and Inconel 625 materials, which are in the hard-to-cut materials class, using standard tungsten carbide micro drills. In this study, the effect of work material and hole depth on feed force, torque, and hole quality (diameter and chip sizes) was examined, and reported that the micro-drillability of hard materials was affected by the ductility of the material rather than the hardness. It has also been emphasized that the hardness of the workpiece and the hole depth mainly affect the tool's life. A slight reduction in hole diameter occurs due to almost constant tool wear after an initial step in which the diameter of the holes is determined. In addition, it was also emphasized that the width and height of the chip removed from the material surface are affected by tool wear, but the material structure only affects the chip width. According to the drilling force results, higher torque values were measured for AISI 310H steel, while lower values were measured for harder materials (i.e., Hastelloy C-22 and Inconel 625).

Tool wear is a severe problem in the machining process of superalloys [25]. For example, Liu et al. [39] subjected Inconel 625 superalloy material to the turning process with PVD-TiAlN coated carbide tools, analyzed the wear morphologies and mechanisms of the tool under different parameters, and created a two-dimensional tool wear map. They reported that the primary wear morphologies of the cutting tool are build-up edge, crater wear, chipping, tipping, and fracturing. In contrast, abrasion, adhesion, and oxidation wear are the main wear mechanisms. Moreover, they also observed that adhesion wear under low-speed cutting yielded a build-up edge wear morphology.

In contrast, adhesion and oxidation wear under high-speed cutting resulted in crater wear. As a result, they concluded that the tool peels, tips, and fractures with increasing cutting speed and feed rate. One of the significant concerns in machinery manufacturing of Ni-based superalloys is machining-induced surface integrity since the surface integrity is closely bound up with the service performance of machined components [40]. Surface metallurgy refers to the microstructural alterations occurring in the machined surface layer, including white layer formation, plastic deformation, grain refinement, etc. [41].

Ni-based superalloys are used in many engineering applications such

Table 1
Typical chemical composition of the deposited WAAM and wrought Inconel 625.

Wrought	**Ni**	**Cr**	**Mo**	**Nb + Ta**	**Fe**	**Ti**	**Al**	**Si**
	min. 58	20–23	8–10	3.15–4.15	max.5.0	max. 0.4	max. 0.4	max. 0.5
	Cu	**Mn**	**C**	**P**	**S**	Co	–	–
	0.01	max. 0.5	max. 0.1	max. 0.015	max. 0.015	max. 1.0	–	–
WAAM	**Ni**	**Cr**	**Mo**	**Nb**[a]	**Fe**[b]	**Ti**	**Al**	**Si**
	65.08	20.48	9.12	4.25	0.54	0.2	0.12	0.06
	Cu	**Mn**	**C**	**P**	**S**	–	–	–
	0.23	0.0	–	0.051	0.073			

[a] Nb content was higher than the maximum limit (of the standard) in all the analyses conducted, and.
[b] Fe content was only higher than the maximum limit in three analyses conducted at the bottom part of the wall structure.

as aerospace, biomedical, agriculture, marine, transportation, vehicle, automotive, railway, defense industry and mining, and they need to be drilled during use in these applications [1,42]. Moreover, manufacturing industries prefer high-quality products with high surface quality, dimensional accuracy, high metal removal rate, and low cost. In this direction, Jayakumar [43] studied the optimization of EDM process parameters such as current, voltage, pulse on time, and electrode profile while applying the Taguchi method to process Inconel 625 alloy with the lowest SR and highest MRR parameters in the EDM method. According to the analysis results, it was emphasized that the current and pulse on-time parameters were very effective on the metal removal rate and surface roughness. Therefore, it was recommended to use a flat electrode for low surface roughness and a fillet-type electrode for high MRR.

Rajguru and Vasudevan [44] studied the processing of Inconel 625 material using TiAlSiN ultra-hard coated solid carbide tool end mill in dry cutting conditions (without the use of coolant), aiming to maximize surface quality and minimize machining costs. In addition, they pointed out that by eliminating the cutting fluid used as a coolant, possible chemical damage to machine operators and the environment would be eliminated. As a result of their analyzes, in order to obtain an excellent SR value between 0.4 and 0.5 μm without using cutting fluid, they recommended machining using the following parameters: feed per tooth between 0.04 and 0.075 mm/tooth, cutting speed 60 to 80 m/min, radial depth of cut 0.2 to 0.7 mm and the radial rake angle in the range of 9°–12°.

In another study, Rajguru and Vasudevan [45] emphasized that Inconel 625 alloy tends to form a hardening layer on the machined surfaces during the end milling operation, which may cause a difficult situation in post-processing use. Therefore, the microhardness of the surface and the substrates up to 200 μm in depth from the surface under dry cutting conditions were analyzed. As a result of the analyses, they reported that the affected area under the machined surface was 70 μm to 80 μm, and the machined surface reached a higher microhardness than the hardness of the base material due to the strain hardening caused by machining.

Khan et al. [46] investigated the effect of magnetic field on MRR, EWR, and R_a when Inconel-625 alloy was processed using Cu electrodes with electrical discharge machining (EDM), namely magnetic-field-assisted EDM (MFA EDM) process. In the experiments, it was tried to create a magnetic field at 0.396 T and 0.665 T densities by using magnets. As a result, low surface roughness (R_a), high MRR, and EWR were obtained owing to less wearing particles (debris) remaining on the machined surfaces by processing in a magnetic field environment. They also reported that with SEM analysis, less cracking occurred on the surface, and they obtained a better-machined surface.

In order to investigate the metallurgical characterization of the machined surface and subsurface, Imran et al. performed the micro-drilling experiments of nickel-base superalloy Inconel 718. These results indicated that an increased cutting speed and feed rate resulted in a slight rise in the WLT [47].

As seen from the literature summary above, Ni-based superalloys are used in many engineering applications such as aerospace, aerospace, biomedical, agriculture, marine, transportation, vehicle, automotive, railway, defense industry, and mining, where perforated machine parts are used [1,42]. Besides, the high heat input and elemental segregation in the WAAM process [48] create differences in the mechanical properties of WAAM alloys compared to wrought Ni-based alloys. When we look at the literature, the fact that a comparative study of the drillability of WAAM and wrought Inconel alloys has yet to be found in the open literature has triggered the emergence of this article. For this purpose, die-sinking micro-EDM, micro-EDM drilling, orbital and conventional drilling methods, and wrought and WAAM materials were comparatively examined in this study. Moreover, the machining characteristics, such as the hole inlet-outlet diameters, dimensional accuracy, kerf angles, surface morphologies, SR of the hole, tool marks inside the hole, and formation of the white layer, which occur in the samples as a result of drilling of Inconel 625 alloys produced by wrought and AM methods with die-sinking micro-EDM, micro-EDM drilling, orbital and conventional drilling methods, have been studied comprehensively and comparatively in this study.

2. Materials and methods

2.1. WAAM process

In this study, Inconel 625 alloy was deposited onto an S304 stainless steel substrate with the size of 12 mm thickness, 75 mm width, and 350 mm length by the WAAM process. In addition, 1.2 mm diameter ER NiCrMo 3 (according to AWS A5.14 and AWS A5.18) filler wire was used in the deposition process. The chemical composition of the wire used is 64.86 wt% Ni, 21.15 wt% Cr, 8.67 wt% Mo, 3.54 wt% Nb, 1.15 wt% Fe, and other impurities.

GeKa-Tec WB 500 L machine with a water-cooled torch integrated into the 6-axis OTC Daihen D-V8L robot was used in the deposition process [17]. The surface of the substrate was cleaned with acetone before the deposition to remove unwanted substances such as oil, dirt, and rust. In the deposition process, the first layer was deposited in a clockwise direction, while the next layer was in a counterclockwise direction; in other words, the deposition directions of the successive layers were reversed. Since the WAAM process directly affects the temperature distribution of wall structures, a dwell time of 120 s was chosen after each layer is deposited to allow the component to transfer excess heat. The deposition process was carried out under 150 A, 15.8 V, and 500 mm/s velocities using a shielding gas of 97.5 % Ar + 2.5 % CO_2 with a flow rate of 15 L/min. Adding 2.5 % CO_2 to the shielding gas for the arc is to stabilize and deeper penetration.

2.2. Characterization of Inconel 625 wall structure fabricated by WAAM

The chemical composition of the WAAM Inconel 625 samples (the average of 9 X-ray fluorescence (XRF) analyses conducted at three different locations, namely bottom, middle and top section, 3 analyses at each location) is given in Table 1. The chemical composition of Wrought Inconel 625 is given based on the quality certificate presented by the Bircelik (Turkey) company from which this alloy was purchased.

Microstructural studies of both wrought Inconel 625 alloy and

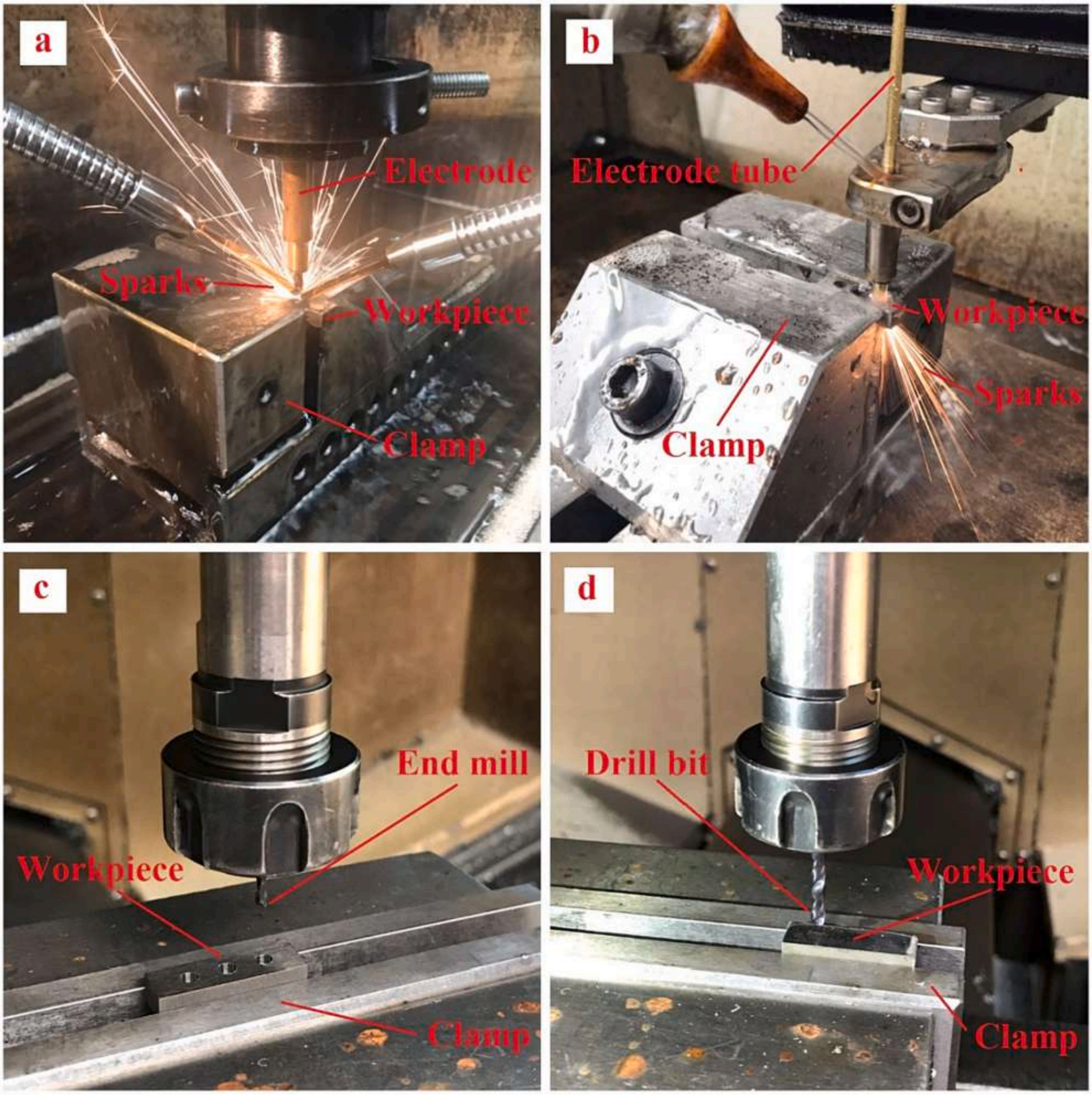

Fig. 1. Manufacturing methods: (a) Die-sinking micro-EDM, (b) Micro-EDM drilling, (c) Orbital drilling, and (d) Conventional drilling.

Inconel 625 samples produced by the WAAM method were performed using a Nikon MA 200 optical microscope. In addition, a Thermo Scientific Apreo S scanning electron microscope (SEM) and energy dispersion spectroscopy (EDS) were used to investigate the microstructure and chemical composition of Inconel 625 specimens. Microhardness measurements with an interval of 0.5 mm were carried out across the wall structure fabricated by WAAM along the building direction to determine the hardness distribution using the Future-Tech FM-700 hardness device (the hardness Vickers (HV) method) under a load of 100 gf and 15 s dwell time. Hardness values are reported based on each sample's average of 20 hardness values.

In order to determine the crystal structures of wrought and WAAM Inconel 625 samples, an X-ray analysis of the samples was performed. For XRD studies, the PANalytical brand, Empyrean model XRD device, which produces CuKα radiation in the range of 2θ = 20–90°, at 40 kV and 30 mA values, was used (λ = 1.5418 Å). In addition, the crystal grain size (D), microstrain (ε), and dislocation density (δ) values of both wrought and WAAM samples were calculated.

The equations given below (Eqs. (1)–(3)) were used to calculate the mean crystal grain size, microstrain, and dislocation density values of the samples [49–51]. Eq. (1) given below, known as the Debye-Scherrer equation, is used to determine grain size [49].

$$D = \frac{0.94\,\lambda}{\beta\, cos\theta} \tag{1}$$

In the Debye-Scherrer Eq. (1), λ: X-ray wavelength, β: the value of half-width of the corresponding most significant peak (FWHM) in radians, θ: Bragg reflection angle of the corresponding peak [46].

Eq. (2) below is used to calculate microstrain [49].

$$\varepsilon = \frac{\beta}{4\, tan\theta} \tag{2}$$

Eq. (3) given below was used to calculate the dislocation density [50,51].

$$\delta = \frac{1}{D^2} \tag{3}$$

Here, D represents the average crystal grain size [51].

2.3. Machining methods

In this study, a total of four different drilling methods, two of which were thermal processes, namely die-sinking micro-EDM, and micro-EDM drilling methods, and the other two being mechanical processes, namely orbital and conventional drilling, were used for machining of wrought and WAAM Inconel 625 alloy specimens, which are in the "difficult-to-cut" materials group and therefore present difficulties in machining. Materials with electrical conductivity can be processed by the EDM method [52]. This method removes chips due to high temperature, and melting is provided utilizing a series of electric sparks between the workpiece and the electrode [53]. The EDM method is sometimes suggested as an alternative process to milling [54]. There are several common types of EDM in the industry, such as die-sinking micro-EDM, wire EDM, and micro-EDM drilling [55].

The die-sinking micro-EDM method uses an electrode with a mirror appearance of the shape to be formed on the workpiece or the hole to be drilled. The erosion process continues until the electrode is fully inserted into the workpiece. Then, the electrode form is removed on the workpiece [52]. In this study, copper electrodes supplied in the form of Ø 10 mm rod (shaft) were turned into rods with Ø 3 mm diameter and 20 mm length on the lathe and used as electrodes. As shown in Fig. 1(a), Eralube brand dielectric liquid was sprayed by spiral metal hoses to evacuate the chips generated between the electrode and the workpiece in the experiments. The erosion process was carried out under dielectric liquid using a Furkan brand EDM machine with 50 Amp power. Machining parameters, 25A current, 60 V voltage, 6 μs arc time, and 6 μs dwell time, machine-safe operating parameters preferred in industrial applications, were used in all drilling operations. These parameters have been determined as relative values considering the following articles and the safe working conditions of the processing machines. The parameters used in previous studies can be summarized as follows. Jayakumar [43] used a 6 mm diameter Cu electrode, 15–25 A current, 50–80 V Voltage 20–40 (μs) T_{on} parameters to process Inconel 625 alloy by EDM method. Baral et al. [56] tried to obtain optimum values by processing Inconel 625 material in the range of 20–30 A and 10–30 V using copper electrodes. They obtained the highest MRR in the experiments with 25 Amper A and 20 V. They stated that it was the optimum parameter, but this could differ according to the electrode diameter, material type, and bench calibration settings. Mishra et al. [35] used 15–25 A and 20–28 V parameters and a copper electrode with a 15 mm outer diameter and 12 mm inner diameter to drill Inconel 625 with the electro-discharge machining method.

In the micro-EDM drilling method, a tubular electrode connected to the chuck is rotated with the help of servo motors and brought closer to the workpiece. As a result, micro-level holes are obtained on the workpiece depending on the electrode diameter [52]. While determining the parameters of the study, publications in the literature on the drillability of wrought alloys were used. Ahmed et al. used 50–140 A, 50 V, 20 μs T_{on}, T_{off} parameters, and 3 different electrodes (Cu, brass, and CuW) for micro-EDM drilling of Inconel 718 alloy [36]. In this study, brass electrode tubes with Ø 3 mm outer diameter and Ø 1.5 mm inner diameter were used for all drilling processes. The experiments were carried out on an Oscarmax SD 400 ZNC PLUS 50 Amp fast-hole drilling EDM (electric discharge machining) machine. In order to evacuate the chips generated between the electrode and the workpiece, the erosion process was carried out under dielectric liquid by spraying dielectric liquid (pure water) from inside the electrode and outside the electrode with spiral hoses, as shown in Fig. 1(b). Considering the brass electrode and machine-safe operating parameters, 7 A current, 29 μs T_{on}, 3 μs T_{off}, and 3 V voltage values were selected and used as operating parameters.

In the orbital drilling process, holes are obtained with the drill moving in the axial direction. In contrast, holes are obtained in the orbital drilling process using end milling cutters that remove chips with movement in both circumferential and axial directions [57]. Considering the published study on the orbital drilling of Ni-based superalloys, Rajguru and Vasudevan [37] used 60–100 m/min cutting speed, 0.04–0.12 mm/tooth feed rate parameters for the end milling of Inconel 625. On the other hand, Venkatesan et al. [44] used 21,000–31,000 rpm, 6–10 mm/min feed rates to drill Inconel 625 Ni alloy with tools in the range of 0.6–0.8 mm. In our study, a higher feed rate and lower spindle speed were used to prevent the tool from breaking since more precise holes were studied (the tool used was 2 mm in diameter). In this study, since WAAM and wrought Inconel 625 workpieces were desired to be drilled, a Ø 2 mm diameter carbide end mill with PF02 × 0.6 × 40 × Z2 dimensions was used as a cutting tool. The workpiece fixed with a special clamp to the Makino S33 model CNC machine, which is used as a workbench, is precisely drilled, as shown in Fig. 1(c). Based on this, the machining parameters were determined as 1000 rpm spindle speed, 150 mm/min cutting feed, and 0.05 mm step depth.

In conventional drilling operations, Tandekar et al. [58] studied the drillability of Inconel 718 material by conventional drilling using 800–1200 (rpm) spindle speed, 0.0375–0.0875 (mm/rev) peck depth, 30–105 feed rate (mm/min) and TiN and TiAlN coated tungsten carbide drill bits. In another study, Khanna et al. [59] used spindle speed 1000 (rpm), peck depth 0.02 (mm/rev), and 6 mm TiAlN coated carbide twist drill parameters, examining the cryogenic drillability of Inconel 718 Superalloy. Considering these studies drilling operations were completed in a Makino S33 model CNC machine equipped with precision clamping systems using Ø 3 × 16 × 46 mm carbide drills with a 118° drill point angle, as shown in Fig. 1(d). A spindle speed of 500 rpm, a 10 mm/min-cut feed, and a peck depth of 0.3 mm was selected as machining parameters. For the evacuation of the abraded particles from the environment and the cooling of the workpiece in the experiments, hangsterfers S-500 was used as a coolant in orbital and conventional drilling processes, whereas eralube (eralube eraoil electron) and distilled water were used in die-sinking micro-EDM and micro-EDM drilling processes, respectively. In the selection of coolants, oxidation resistance, being completely harmless from a physiological point of view, being produced from unique hydrocarbon compounds, and thus not harming the personnel (operator) and the machine has been the reasons for preference. In addition, the selected coolants showed a better washing effect in very thin sections due to their low viscosity and easily removing the formed erosion particles from the erosion zone. Therefore, the working parameters used in all the experiments were primarily considered with respect to the literature studies on superalloys. Then the machine's safe working conditions and the results obtained in the preliminary trials were determined according to these considerations.

2.4. Analysis methods of machining quality

All the test materials prepared after each drilling process were cleaned with dielectric fluid from slag residues using high-pressure air before kerf analysis. Then, the workpiece's hole entry and exit dimensions were determined using a Mitutoyo caliper. For each hole diameter, 3 measurements were made, and average values were reported. As a result of the measurements made, it was seen that the hole inlet diameters were larger than the hole outlet diameters. Thus the kerf angle was formed. The equation given in Eq. (4) was used to calculate the kerf angle formed [60].

$$Kerf\ Taper\ Angle\ (\ T\ ) = \mathrm{Arctan}\left(\frac{H_{en} - H_{ex}}{2.t}\right) \tag{4}$$

In this equation, H_{en} is the hole entry diameter of the electrode/cutting tool when entering the workpiece, and H_{ex} is the hole exit diameter the tool creates when it exits the workpiece. The workpiece

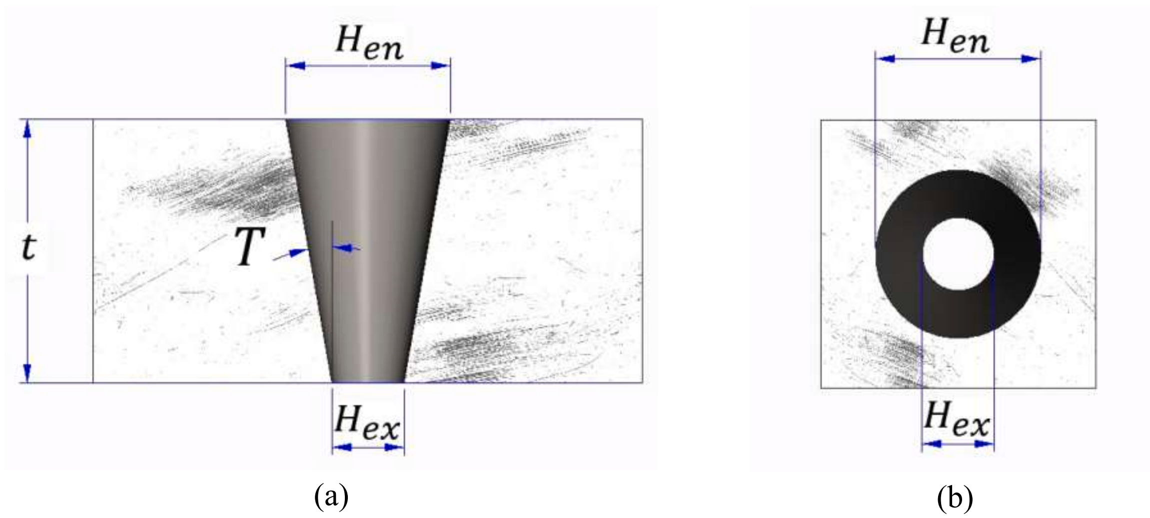

Fig. 2. Measurements of the kerf taper angle: (a) hole section view and (b) hole top view.

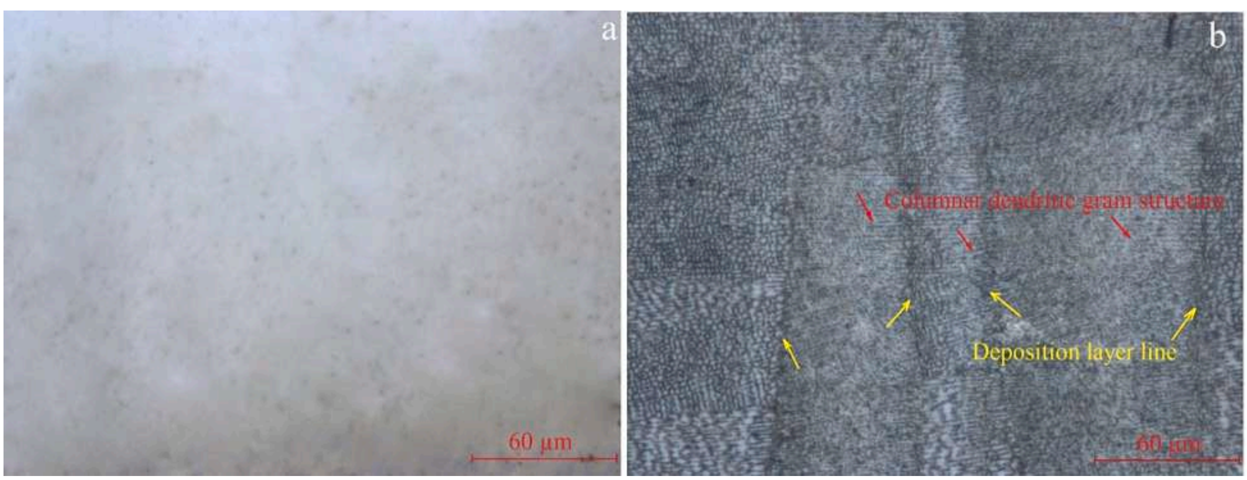

Fig. 3. OM views of Inconel 625 specimens: a) wrought and b) additively manufactured.

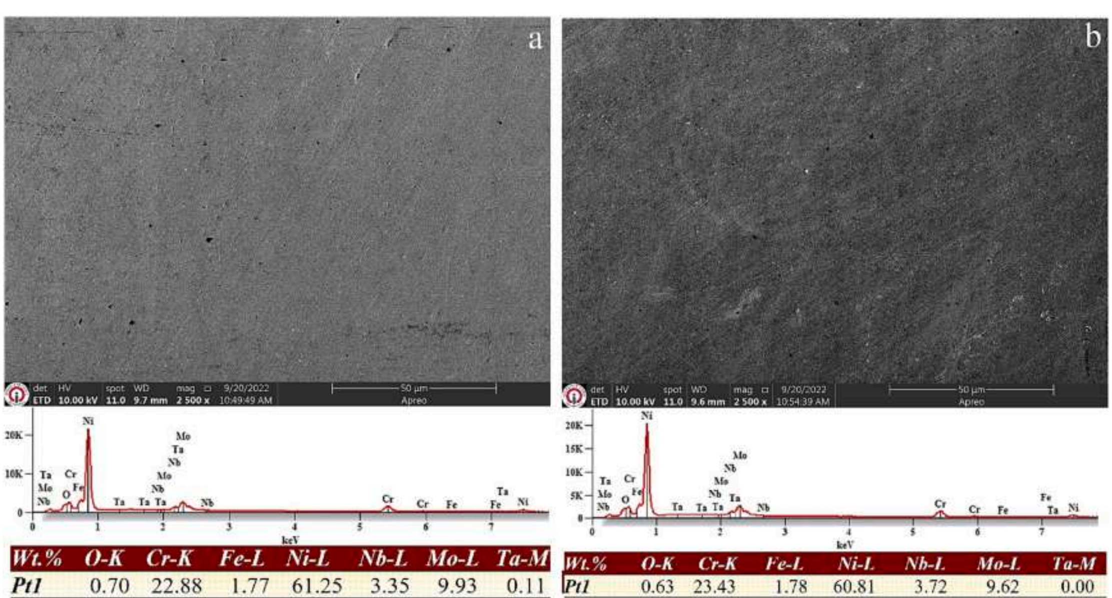

Fig. 4. Cross-section SEM views and EDS analysis results of Inconel 625 alloys: a) wrought and b) additively manufactured.

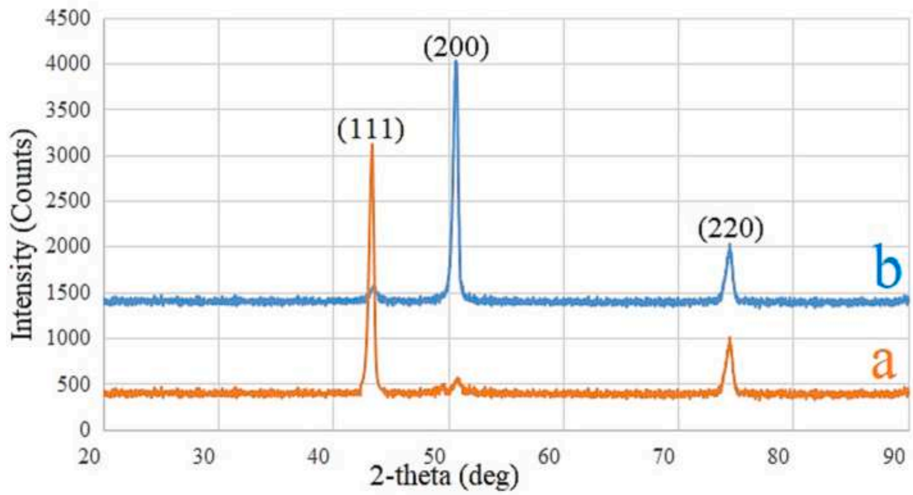

Fig. 5. X-ray diffraction patterns of Inconel 625 alloys: a) wrought and b) additively manufactured.

Table 2
Variables obtained from XRD images of wrought and additively manufactured Inconel 625 samples.

Specimen	2θ (degrees)	FWHM-β (radians)	Average grain size, D (nm)	Microstrain, ε	Dislocation density, δ (nm^{-2})
Wrought	43.660	0,004886	31.95	3.049×10^{-3}	0.979×10^{-3}
WAAM	50.652	0,007923	20.23	4.185×10^{-3}	2.443×10^{-3}

Table 3
Kerf measurement values.

Drilling method	Inconel 625	Hole entry diameter (mm)	Hole exit diameter (mm)	Thickness (mm)	Kerf (degree)
Die-Sinking	WAAM	3.30	3.15	5.00	0.859
Micro-EDM	Wrought	3.18	3.08	5.00	0.572
Micro-EDM	WAAM	3.48	3.44	5.00	0.229
Drilling	Wrought	3.40	3.38	5.00	0.114
Orbital	WAAM	3.06	3.04	5.00	0.114
Drilling	Wrought	3.04	3.03	5.00	0.057
Conventional	WAAM	3.01	2.98	5.00	0.171
Drilling	Wrought	3.01	2.99	5.00	0.114

thickness t is the same in all experiments and is 5 mm. The kerf angle, T, caused by the hole inlet and outlet differences is shown in Fig. 2.

All test specimens drilled with different methods were cut into two halves from their mid-points on the WEDM workbench, and the SR values of the inner walls of the holes were measured by Huvitz HDS-58003D profiling (Republic of Korea) device at a speed of 0.1 mm/s and a length of 4.8 mm, and their 3D appearance was obtained. R_a (μm), R_z (μm), and R_{max} (μm) values were determined for the roughness determination of each of the drilled surfaces. In addition, the final values were obtained by taking the average of five different measurement values for the SR of each drilled surface.

The dimensional accuracy of the drilled holes was determined with an optical microscope. Then, the inner parts of the drilled holes were examined with EDS utilized on an SEM to determine the microstructure and chemical composition on the surface. Next, the drilled surfaces were examined in detail to determine the presence of cracks, voids, globules, craters, and debris. Finally, with the EDS analyses taken from different areas of the hole surfaces, the effect of different drilling methods on the material and the worn workpiece, electrode, and cutting tool residues on the machined surfaces were tried to be determined.

The drilled holes were cut in two halves with WEDM right in the middle, and the cross-sectional surfaces of the holes were polished by grinding with 320–2500 SiC sandpapers. In order to determine the white layer or cold deformation effects occurring depending on the drilling method. The thickness of the formed white layer was measured using Image Pro Plus 6 software. 3 different cross-sectional SEM views were used, and 5 thickness measurements were taken from each SEM view to calculate the average white layer thickness. Moreover, the microhardness values of the samples were measured along a line starting from the surface down to 100 μm depth on the hole cross-section surfaces with a load of 100 gf and 15 s loading time with a Future-TECH brand FM-700 Vickers microhardness device using a diamond tip. And then, the obtained hardness indentations were examined with an optical microscope.

3. Results and discussions

3.1. Microstructure and XRD analysis findings

The optical microscope image of the commercially obtained wrought Inconel 625 alloy and the Inconel 625 sample fabricated by the WAMM process is presented in Fig. 3. The SEM image and EDS analysis results are shown in Fig. 4.

As seen in Fig. 3, wrought Inconel 625 alloy has a homogeneous microstructure mainly composed of austenite matrix but also contains secondary phases in places (black areas). On the other hand, the microstructure of the Inconel 625 sample produced with WAAM is a columnar dendritic structure containing distinctive deposition layer lines (yellow arrows), and it is a more heterogeneous structure compared to that of the wrought alloy. It was reported by Yangfan et al. [61] that this heterogeneity in the microstructure of the specimen fabricated by the WAAM process may be caused by the cooling rate and heat dissipation during layer deposition. However, as seen in the EDS analyses shown in Fig. 4, the chemical compositions of the wrought and WAAM samples were found to be quite close to each other. This shows that the parameters used for the wall structure production process by the WAAM process and the wire selection are appropriate.

Fig. 5 shows the X-ray (XRD) patterns of both wrought and additively manufactured Inconel 625 alloys.

The XRD analyses conducted on the samples (Fig. 5) determined that both wrought and WAAM samples had only FCC γ Cr-Ni-Fe structure. However, the main dominant peak of the wrought material was the (1,1,1) peak at 43.66°, while in the WAAM sample, the (2,0,0) peak at

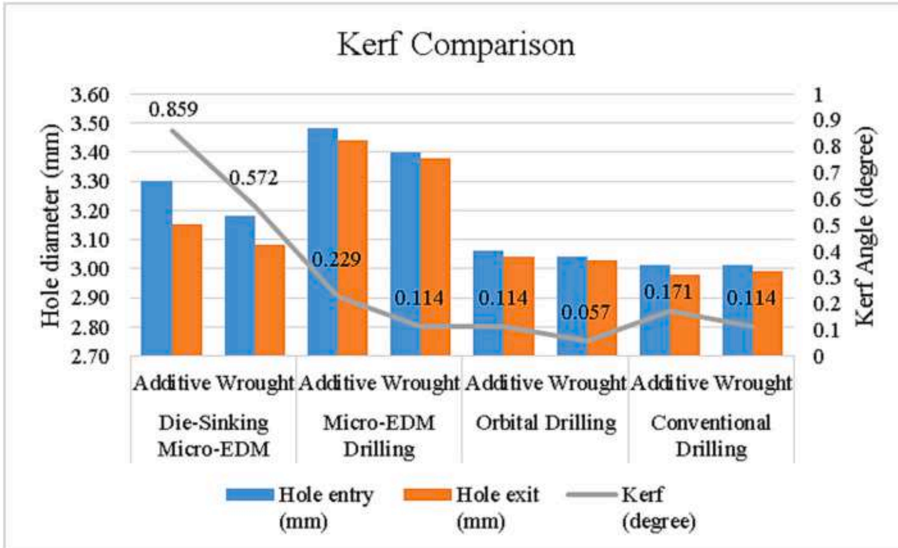

Fig. 6. Measurements of the kerf taper angle for all the drilling methods used.

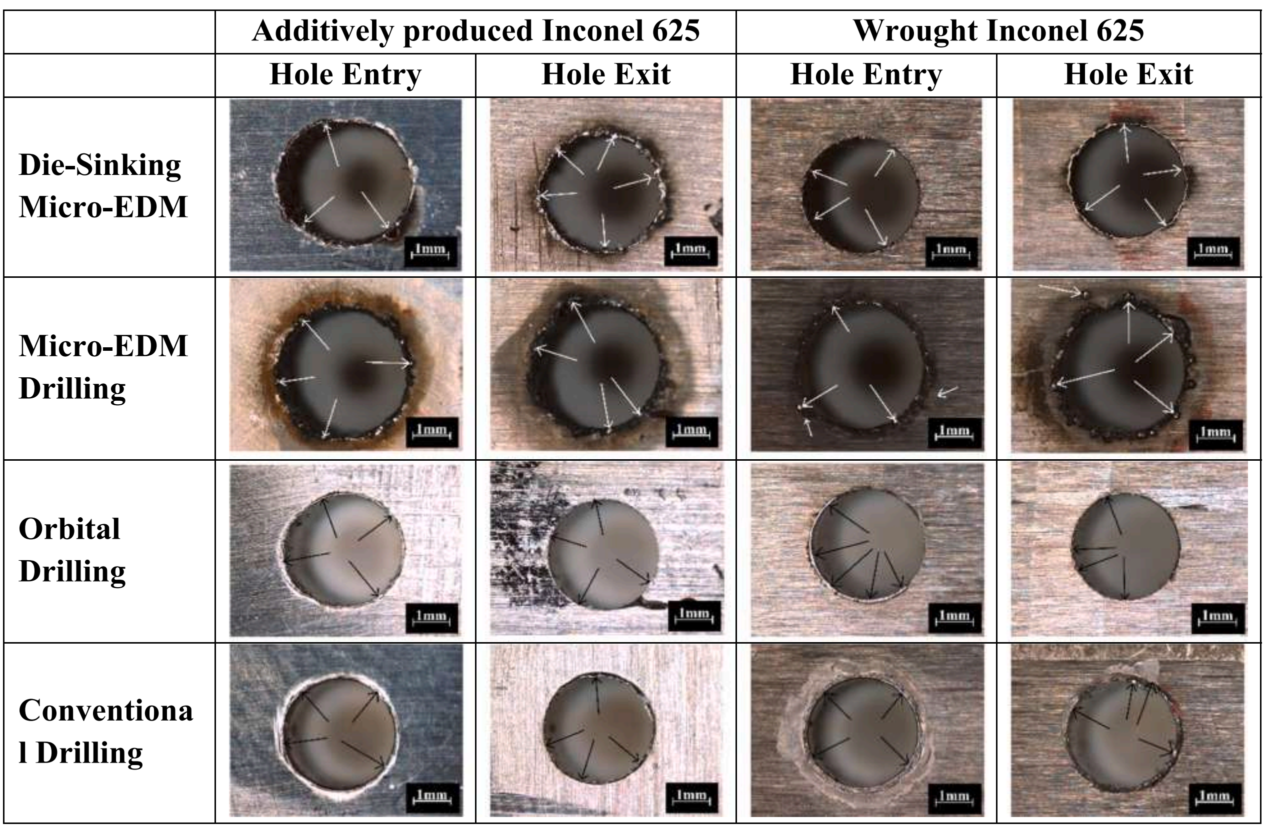

Fig. 7. Hole entry-exit macro analysis by Nikon SMZ 745 T optical microscope.

50.65° was found to be the highest intensity peak. Considering XRD results in Fig. 5, it is seen that the peak intensities of WAAM samples and wrought Inconel 625 showed differences due to the dominant crystallographic orientation of the grains. This situation can be explained as follows: Epitaxial growth is dominant in Inconel alloys produced by AM, in which {100} grain growth is the preferential orientation for FCC structures [62]. Therefore, after grain orientation stabilized in {100} direction, epitaxial growth promoted strong {100} crystallographic orientation, thus resulting in strong (200) peaks in the XRD pattern of WAAM samples. In Wrought samples, on the other hand, (111) orientation is more dominant since deformation-induced twin formation and subsequent recrystallization occurred [19]. These findings agree with the results reported in the open literature [19,62]. Therefore, according to the results of the microhardness values taken from the samples, it was determined that the hardness of the WAAM sample was 402 ± 20 HV. In contrast, the hardness value of the wrought material was 435 ± 47 HV. The hardness values of the samples produced with WAAM are slightly lower than the hardness of the forged samples may be due to the columnar dendritic structure because these structures cause regional discontinuities in the microstructure. This can also be understood from

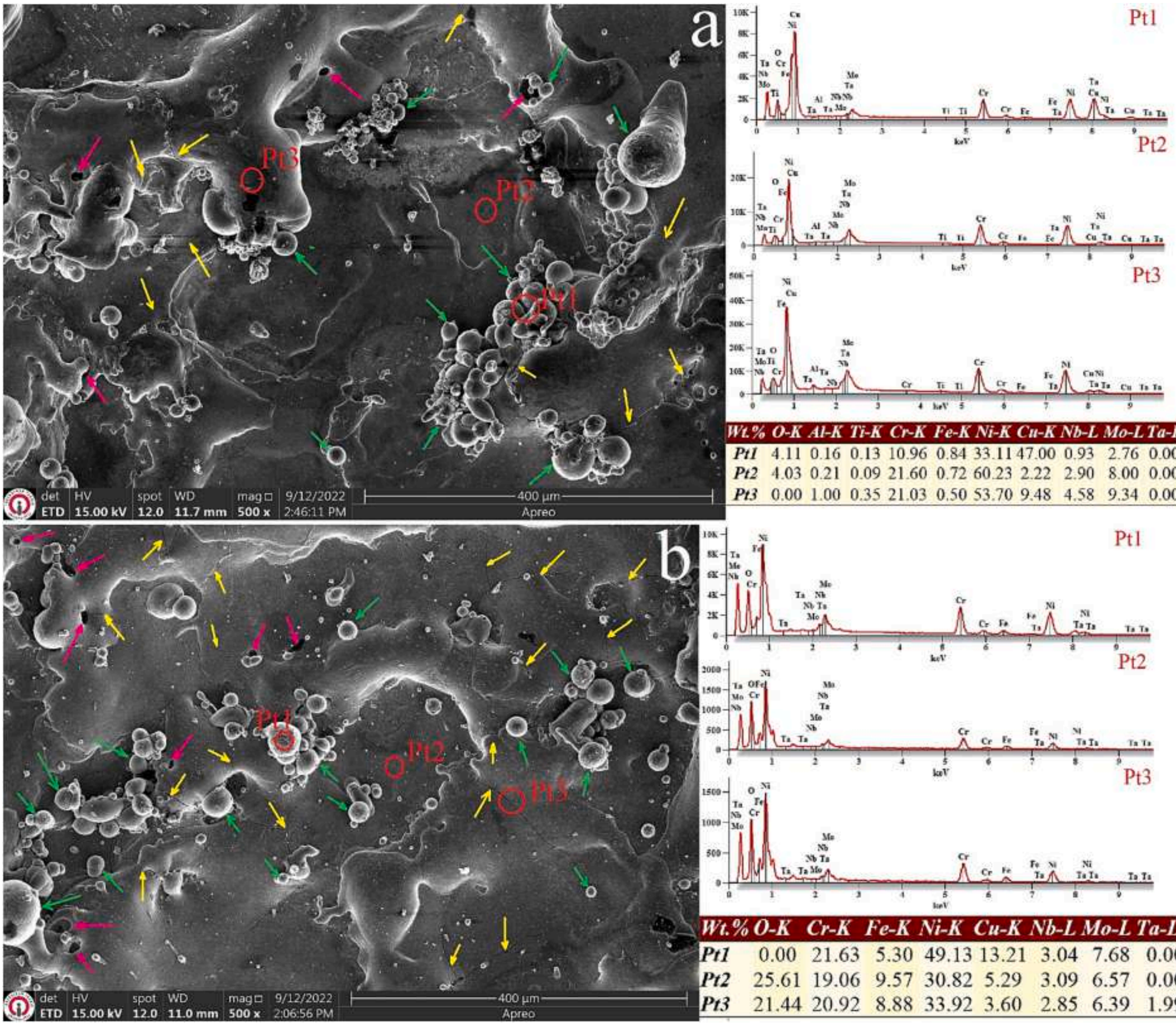

Wt.%	O-K	Al-K	Ti-K	Cr-K	Fe-K	Ni-K	Cu-K	Nb-L	Mo-L	Ta-L
Pt1	4.11	0.16	0.13	10.96	0.84	33.11	47.00	0.93	2.76	0.00
Pt2	4.03	0.21	0.09	21.60	0.72	60.23	2.22	2.90	8.00	0.00
Pt3	0.00	1.00	0.35	21.03	0.50	53.70	9.48	4.58	9.34	0.00

Wt.%	O-K	Cr-K	Fe-K	Ni-K	Cu-K	Nb-L	Mo-L	Ta-L
Pt1	0.00	21.63	5.30	49.13	13.21	3.04	7.68	0.00
Pt2	25.61	19.06	9.57	30.82	5.29	3.09	6.57	0.00
Pt3	21.44	20.92	8.88	33.92	3.60	2.85	6.39	1.99

Fig. 8. SEM images of the machined surfaces by the die-sinking micro-EDM method: (a) wrought and (b) additively manufactured. (Note: yellow arrows indicate microcracks formation, pink arrows indicate voids formation, and green lines indicate globule formation.) (For interpretation of the references to colour in this figure legend, the reader is referred to the web version of this article.)

the fact that the standard deviation in the hardness measurements of WAAM samples is higher than that of wrought.

Information such as average grain size (D), microstrain (ε), and dislocation density (δ) values of the samples, which are of great importance for machinability, can also be obtained in XRD analysis besides obtaining information about the phase structure of the materials. Table 2 was prepared using the XRD graphics presented in Fig. 5 and the equations in Section 2.2. Table 2 summarizes the variables obtained from XRD images of wrought and additively manufactured Inconel 625 samples are summarized.

When Table 2 is examined, it can be seen that the average grain size (20.23 nm) of the sample produced with WAAM is smaller than the wrought material (i,e, 31.95 nm). However, the microstrain and dislocation density values are higher. This situation is thought to be caused by the cooling-heating cycles between successive deposition processes in the WAAM method, as seen from the optical micrograph in Fig. 3.

3.2. Cutting parameters and key findings

The values obtained after the hole inlet and outlet measurements are given in Table 3. As seen in Table 3, it was observed that the hole inlet diameter values were larger than the hole exit diameters in all hole drilling methods. This is due to the wear of the electrode and cutting tool used in the drilling processes, as pointed out by [63]. On the other hand, it was determined that this difference was higher in samples produced with WAAM, resulting in higher kerf angles (Table 3). This results from the severer cutting tool wear due to the higher hardness value of the WAAM-produced samples compared to the wrought samples.

Similarly, it has been stated in Ref. [64,65] that tool wear was detected on the cutting tips and edges of the cutting tool (lateral face and frontal plane) as a result of drilling hard-to-cut materials, such as Ni-based superalloys, and the wear of the cutting tool increased with the increase in workpiece hardness. In addition, it has been reported that the hard second-phase particles in the drilled material increase the material strength and hardness. However, they also cause tool wear in methods such as milling, orbital and conventional drilling [65].

The lowest kerf angle was obtained in orbital drilling due to end mills with butt and edge cutting capability. Conventional drilling, micro-EDM, and die-sinking methods respectively followed this. The highest kerf values were determined due to copper and brass electrode wear in the holes drilled with EDM methods based on the thermal hole drilling principle. The reason for this situation is the intense sparking between the electrode and the workpiece and the discharge (removal) of the electrode form in the workpiece by melting and evaporation in EDM methods. Therefore, the electrode measurements at the beginning of the erosion and the end of the process are not the same. Due to thermal effects, the electrode tips wear more, which increases the Kerf formation on the workpiece [63]. In the die-sinking method, the kerf angle is at the

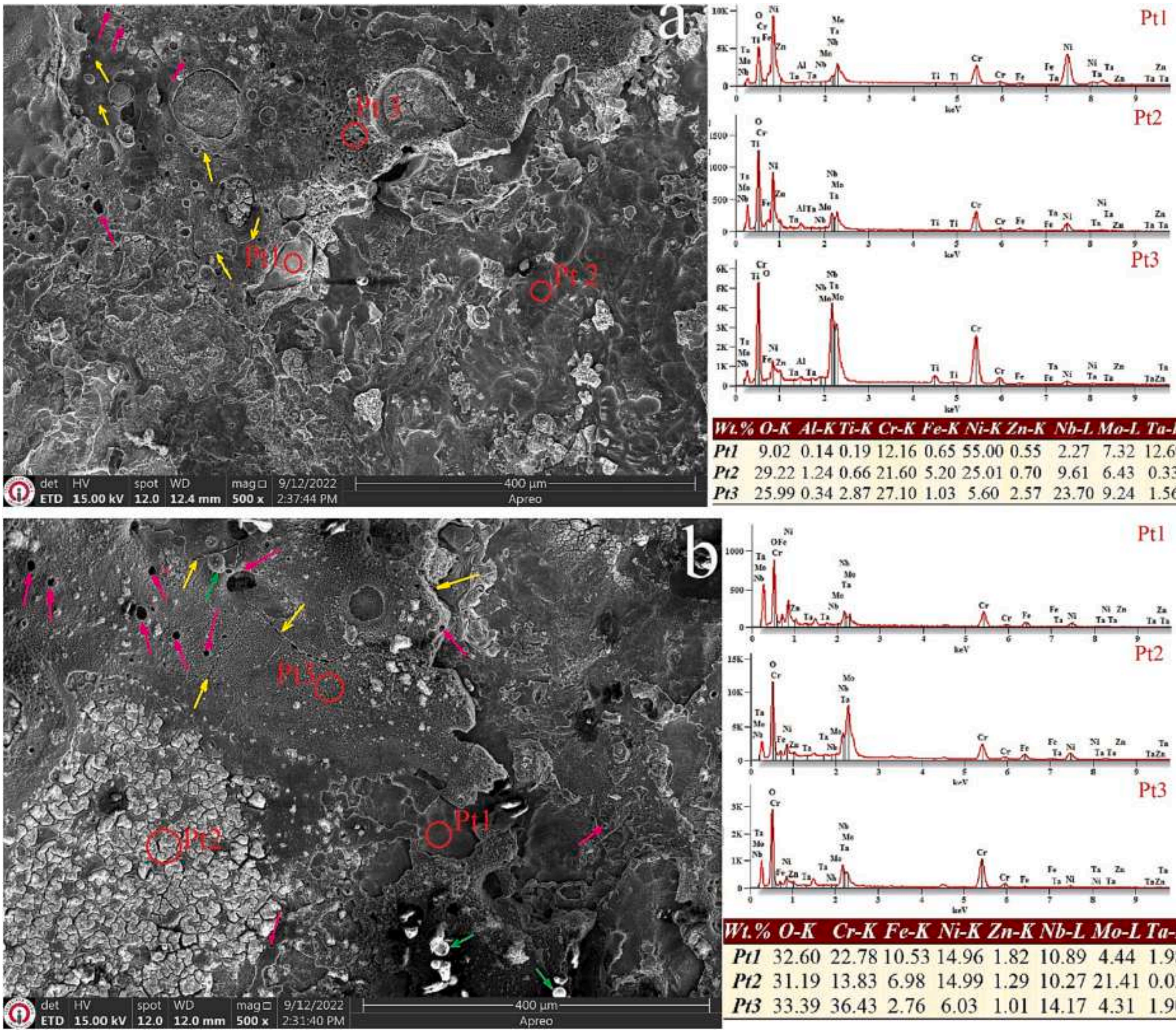

Wt.%	O-K	Al-K	Ti-K	Cr-K	Fe-K	Ni-K	Zn-K	Nb-L	Mo-L	Ta-L
Pt1	9.02	0.14	0.19	12.16	0.65	55.00	0.55	2.27	7.32	12.69
Pt2	29.22	1.24	0.66	21.60	5.20	25.01	0.70	9.61	6.43	0.33
Pt3	25.99	0.34	2.87	27.10	1.03	5.60	2.57	23.70	9.24	1.56

Wt.%	O-K	Cr-K	Fe-K	Ni-K	Zn-K	Nb-L	Mo-L	Ta-L
Pt1	32.60	22.78	10.53	14.96	1.82	10.89	4.44	1.98
Pt2	31.19	13.83	6.98	14.99	1.29	10.27	21.41	0.03
Pt3	33.39	36.43	2.76	6.03	1.01	14.17	4.31	1.90

Fig. 9. SEM images of the machined surfaces by the micro-EDM drilling method: (a) wrought and (b) additively manufactured. (Note: yellow arrows indicate microcracks formation, pink arrows indicate voids formation, and green lines indicate globules formation). (For interpretation of the references to colour in this figure legend, the reader is referred to the web version of this article.)

highest value because the processing current and processing time are high. In micro-EDM drilling, the tube-shaped electrode is connected to the system with the help of the chuck and rotates at about 1000 rpm [66]. Since the electrode material connected to the chuck rotates continuously, the hole inlet-outlet diameters are high due to the balance. However, the electrode wear and naturally the kerf angle are lower than the die-sinking method because the processing time is very short as shown Fig. 6.

The macrographs of the hole entrance and exit regions obtained by optical microscope (Nikon SMZ 745 T) from the samples drilled with four different drilling methods employed are given in Fig. 7.

Since heating and melting with an arc are used for chip removal in die-sinking micro-EDM and micro-EDM drilling methods, molten material residues were observed at the hole entry and exit edges. Molten material residues are shown with white arrows in Fig. 7. On the other hand, in orbital drilling and conventional drilling method, cutting chips and cutting tool traces were present on the hole-entry and exit edges, as the chip is mechanically removed from the workpiece in these methods by using the sharp edges of the cutting tool. These cutting tool marks (deformations) are shown with black arrows in Fig. 7. When the macrographs of the samples produced with WAAM and the wrought materials are compared, it is noteworthy that the hole qualities obtained in the wrought material are higher. This can be attributed to the wrought material's lower hardness, making it easier to undergo plastic deformation in orbital drilling and conventional drilling methods compared to the WAAM specimens. The lower microstructural homogeneity of the samples produced with WAAM may have caused this situation since the drilling process can be conducted without being affected by hardness in die-sinking micro-EDM and micro-EDM drilling methods. It is seen that the samples produced with the WAAM process have higher strain and dislocation density (Table 2).

In order to examine the hole surface morphologies of the samples drilled with different methods, the cut surfaces of the samples were investigated in detail by SEM and EDS analyzes (Fig. 8-Fig. 15).

When the images taken from the hole surfaces of the samples drilled by die-sinking micro-EDM and micro-EDM drilling methods were examined (Fig. 8 and Fig. 9), crack and void formations were observed on the surface in both methods, it was observed that globules formations were only detected in the samples drilled by the die-sinking micro-EDM method. The fact that globules formations were not observed in the micro-EDM drilling method, while the melting and solidifying layer (black zone) were formed in a larger area on the surface, is because the micro-EDM drilling method causes higher temperature formation in the material than the die-sinking micro-EDM method [67]. Because, in the micro-EDM drilling method, there is a certain speed of rotation of the electrode and at the same time, pure water is sprayed inside and outside the electrode. Therefore, the melted material immediately solidifies and is evacuated from the environment [67]. High heat, sparks, melting, gas,

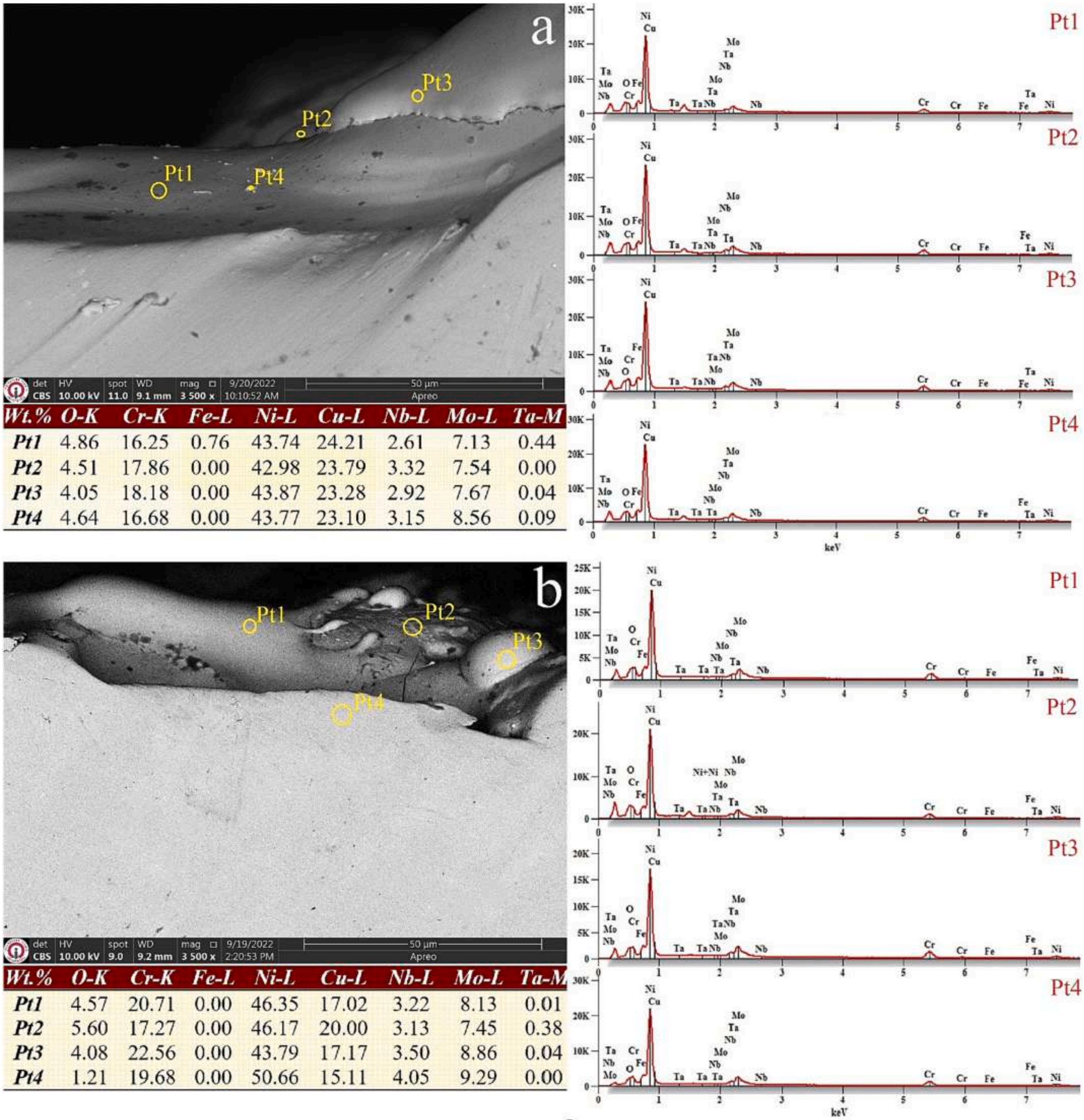

Fig. 10. Recast layer formation in die-sinking micro-EDM: (a) wrought and (b) additively manufactured alloy.

smoke and pure water spraying in the method cause the formation of blackened areas on the hole edges.

On the other hand, the formation of globules, craters, and voids on the surface directly affects the surface morphology [68]. The gases trapped during the solidification of the metal melted at high-temperature form ‘globules’. If these globules burst during solidification, they form voids. These voids and globules formed on the surface are larger than craters and debris, and these defects form as a result of the solidification of the melted material on the machined surface before it is completely removed from the surface. When the SEM surface micrographs given in Figs. 8 and 9 were examined, and it was determined that cracks, voids, globules, craters, and debris formations were observed in both the wrought and WAAM samples, but especially the microcracks and voids formations were more intense in the WAAM-produced sample. This resulted from the higher strain and dislocation density of the samples produced by the WAAM process. Because the heating-cooling cycles that occur during the successive deposition of layers in the WAAM process are higher than that of wrought alloy, causing irregularities during drilling.

The oxide layer (re-cast layer) on the workpiece and the electrode is known to be formed by the conversion of water-based dielectric fluids into hydrogen and oxygen as a result of chemical reactions, which are used to evacuate the workpiece and electrode material debris that are abraded and/or evaporated under high temperatures during drilling

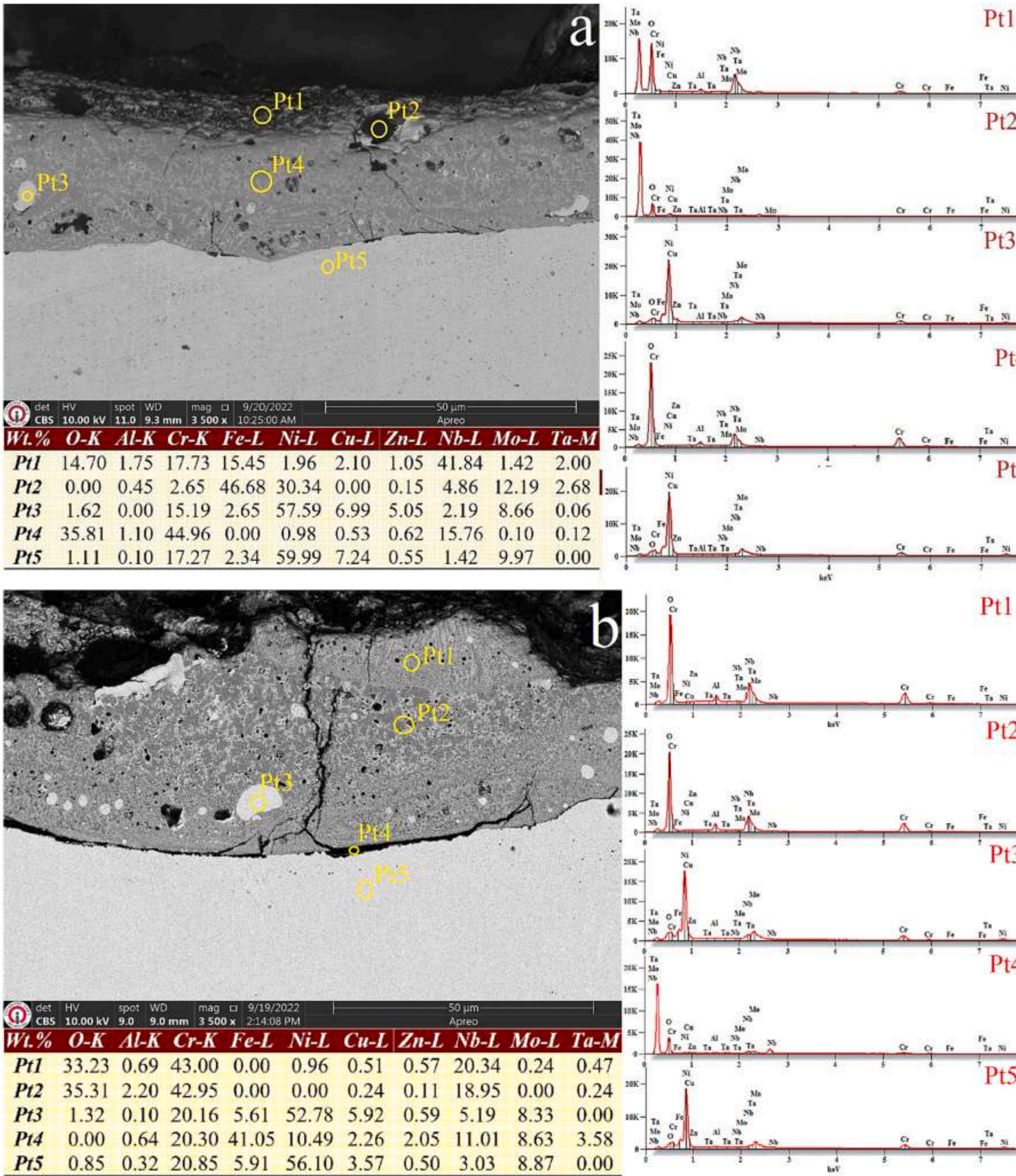

(a)

Wt.%	O-K	Al-K	Cr-K	Fe-L	Ni-L	Cu-L	Zn-L	Nb-L	Mo-L	Ta-M
Pt1	14.70	1.75	17.73	15.45	1.96	2.10	1.05	41.84	1.42	2.00
Pt2	0.00	0.45	2.65	46.68	30.34	0.00	0.15	4.86	12.19	2.68
Pt3	1.62	0.00	15.19	2.65	57.59	6.99	5.05	2.19	8.66	0.06
Pt4	35.81	1.10	44.96	0.00	0.98	0.53	0.62	15.76	0.10	0.12
Pt5	1.11	0.10	17.27	2.34	59.99	7.24	0.55	1.42	9.97	0.00

(b)

Wt.%	O-K	Al-K	Cr-K	Fe-L	Ni-L	Cu-L	Zn-L	Nb-L	Mo-L	Ta-M
Pt1	33.23	0.69	43.00	0.00	0.96	0.51	0.57	20.34	0.24	0.47
Pt2	35.31	2.20	42.95	0.00	0.00	0.24	0.11	18.95	0.00	0.24
Pt3	1.32	0.10	20.16	5.61	52.78	5.92	0.59	5.19	8.33	0.00
Pt4	0.00	0.64	20.30	41.05	10.49	2.26	2.05	11.01	8.63	3.58
Pt5	0.85	0.32	20.85	5.91	56.10	3.57	0.50	3.03	8.87	0.00

Fig. 11. Recast layer formation in micro-EDM drilling: (a) wrought and (b) additively manufactured alloy.

with thermal methods such as EDM (electro discharge machining) [36]. In EDM methods, molten debris breaking off the workpiece surface may not be evacuated with dielectric liquid from the environment, due to the fact that the dielectric liquid cannot reach the cutting area quickly. In this case, the eroded particles (debris) re-solidify in the 'recast layer' and form this region [69]. In the micro-EDM drilling method, it was determined by analytical measurements in Table 3 and Fig. 6 that the hole entrance and exit dimensions of the work material are the highest compared to other methods. This is due to the sudden cooling of the debris braking off the melted workpiece surface by the coolant and solidifing by adhering to the inner wall of the hole (Figs. 10 and 11). As can be seen in Figs. 10 and 11, a recast layer of 35 and 50 μm thick was formed in the hole sections of the wrought and WAAM samples drilled by micro-EDM drilling method, respectively, while the recast layer was measured as 20 and 25 μm, respectively, for the wrought and WAAM samples drilled by die-sinking micro-EDM method. The fact that the black region that melted and solidified in the micro-EDM drilling method was formed in a larger area, was also supported by the EDS analyzes. Due to the higher dislocation density of the samples produced with WAAM (Table 2), a higher rate of cracks detected on their surfaces (Figs. 8 and 9) were also seen in the cross-sectional views, and it was determined that the vertical cracks in the WAAM samples continued throughout the white layer. (Figs. 10b and 11b). This is related to the higher dislocation densities of WAAM samples detected from XRD analyzes as mentioned before (Table 2).

In Figs. 12 and 13, SEM images and EDS analyses taken from the surface of the holes drilled with orbital drilling and conventional drilling methods are presented, while SEM micrographs and EDS analyses of the cross-sections of these holes are presented in Figs. 14 and 15.

As seen in Figs. 12 and 13, the surfaces of the holes drilled with

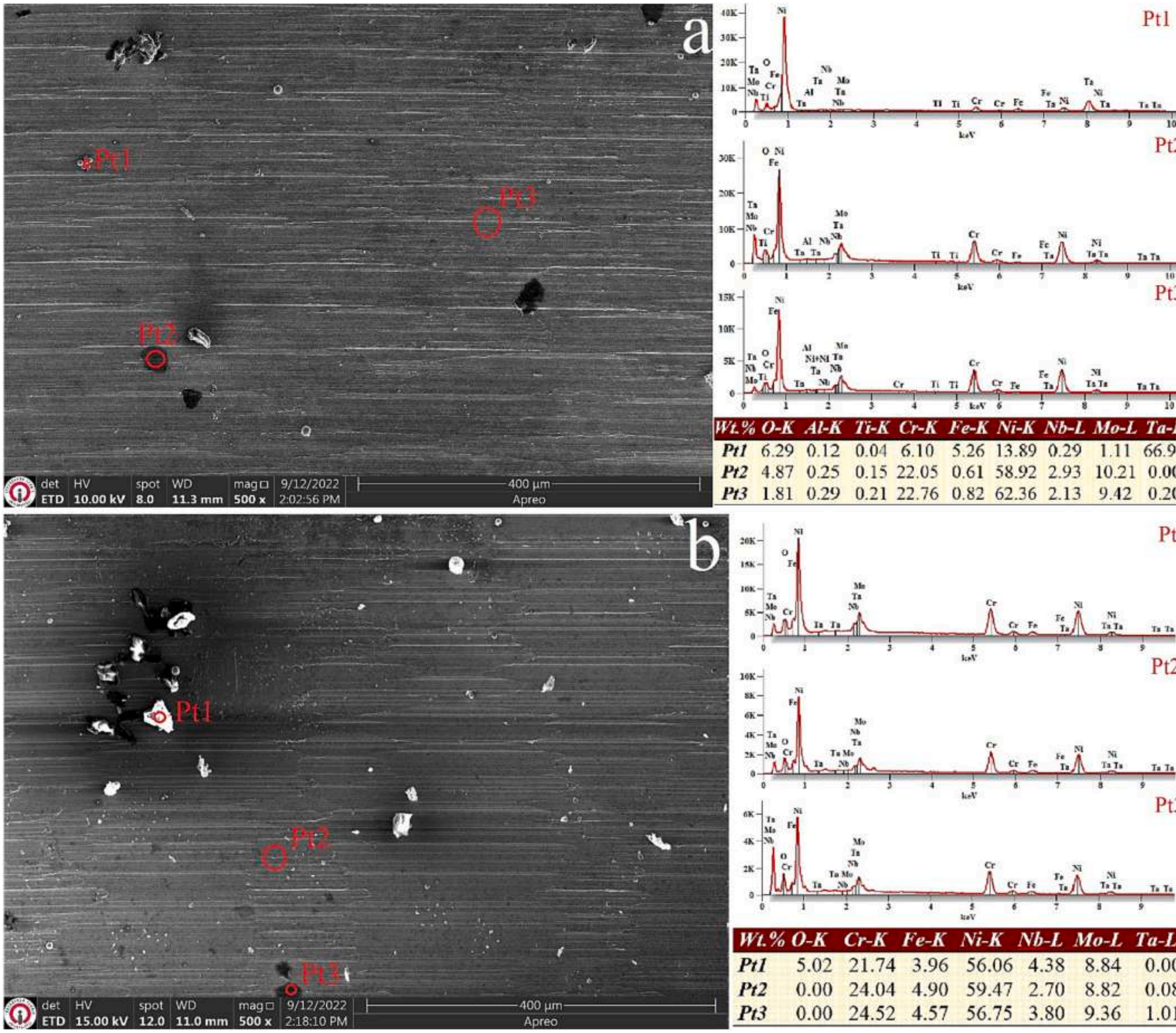

Wt.%	O-K	Al-K	Ti-K	Cr-K	Fe-K	Ni-K	Nb-L	Mo-L	Ta-L
Pt1	6.29	0.12	0.04	6.10	5.26	13.89	0.29	1.11	66.90
Pt2	4.87	0.25	0.15	22.05	0.61	58.92	2.93	10.21	0.00
Pt3	1.81	0.29	0.21	22.76	0.82	62.36	2.13	9.42	0.20

Wt.%	O-K	Cr-K	Fe-K	Ni-K	Nb-L	Mo-L	Ta-L
Pt1	5.02	21.74	3.96	56.06	4.38	8.84	0.00
Pt2	0.00	24.04	4.90	59.47	2.70	8.82	0.08
Pt3	0.00	24.52	4.57	56.75	3.80	9.36	1.01

Fig. 12. SEM image of the machined surface by the orbital drilling method: (a) wrought and (b) additively manufactured alloy.

orbital drilling and conventional drilling methods are much cleaner and clearer than those obtained in die-sinking micro-EDM and micro-EDM drilling methods (Figs. 8 and 9). A melted and solidified structure (black region) was not observed in Figs. 12 and 13, and the surface had a smoother appearance. In addition, abrasive wear lines and wear debris were observed along the surface. This difference in the surface is a result of the fact that the orbital drilling and conventional drilling methods are based on the mechanical removal of chips from the workpiece through the sharp edges of the cutting tools, and therefore, the melted and solidified zone called the re-cast layer is not formed in these methods. For this reason, no recast layer was observed in the SEM images (Figs. 14 and 15) taken from the cross-sectional view of the samples. In these methods, chips are removed by mechanical force generated by linear and circular motion of the tool on the material, generally by creating plastic deformation and shear stresses in the material [53]. Therefore, the surfaces are shiny and smooth as shown in Figs. 12 and 13. There are helical grooves on the drill and milling cutter to remove the chips from the workpiece during drilling. If the chips coming out of these channels rub against the inner surface of the hole, they will scratch the surface, and tool marks will form as shown in Figs. 12 and 13.

When the wrought and WAAM samples are compared, it is clearly seen from Fig. 12 that these scratches are deeper on the surface of the wrought samples. This is related to the higher hardness values of the samples fabricated by WAAM. Because the harder the material, the higher the plastic deformation resistance to the abrasive that tries to scratch (worn) it [70,71]. Another proof that a recast layer does not form in orbital drilling and conventional drilling methods is that the oxygen values in the EDS analyses on these samples were determined as “0” in areas other than polluted spots (Pt2 in Fig. 14a and Pt2 in Fig. 15b). When orbital drilling and conventional drilling are compared, it has been observed that the abrasive wear marks on the wrought material are deeper as a result of the application of more force during the conventional drilling method compared to the orbital drilling process. On the other hand, although the surface was smoother in the conventional drilling method in the WAAM sample, it was observed that fractures occurred in some areas. This is thought to be due to the lower fracture toughness of the WAAM specimen due to its higher hardness and higher dislocation density [72].

The SR values (R_a, R_z, R_{max}) measured from the hole surfaces of the samples drilled with four different methods are summarized in Fig. 16.

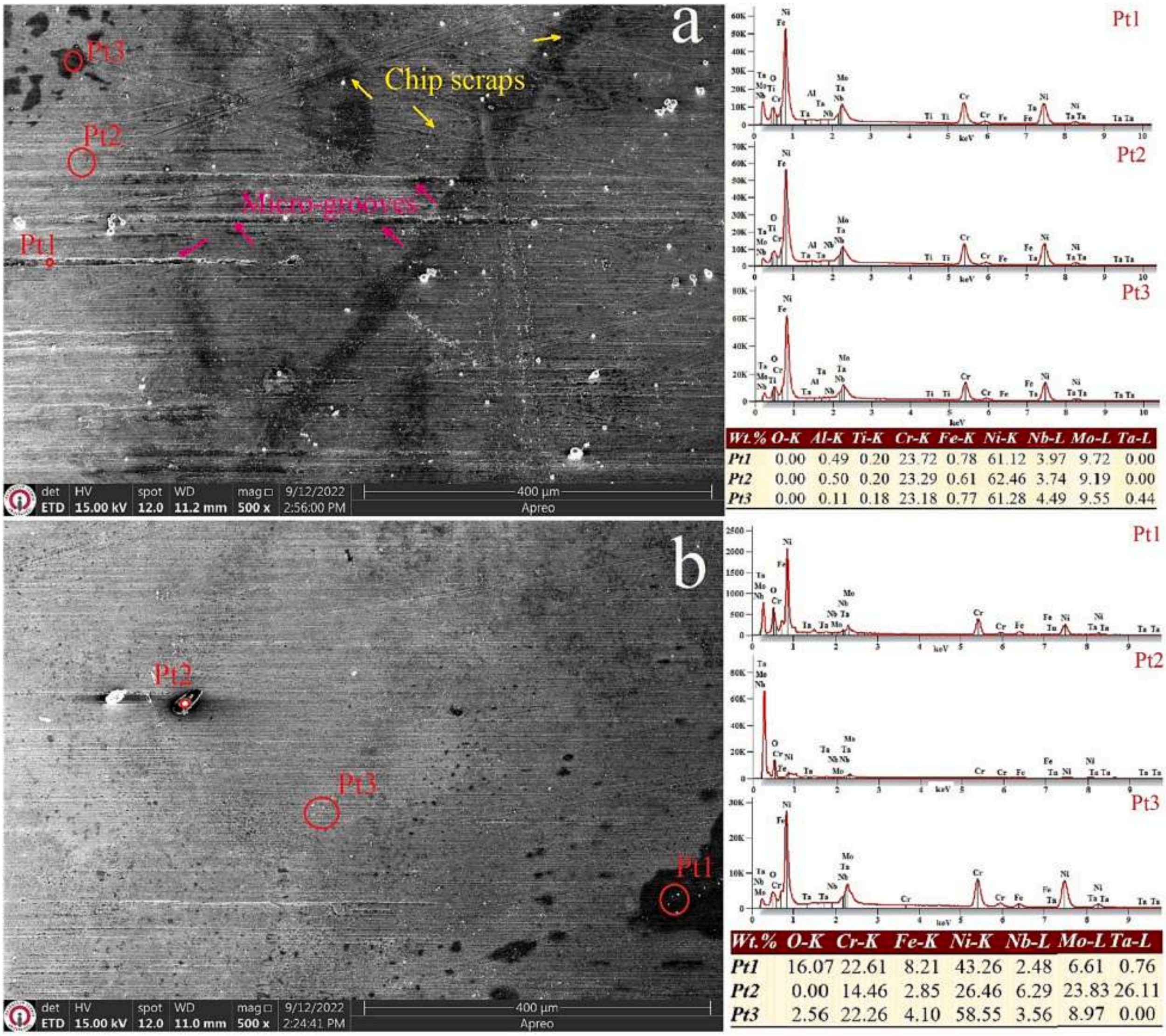

Fig. 13. SEM image of the machined surface by the conventional drilling process: (a) wrought and (b) additively manufactured alloy.

The arithmetic mean deviation, R_a, of the profile evaluated here, the mean of the profile's greatest height values, R_z, and the maximum roughness depth, R_{max}, are given as the SR parameters defined in ASME B46.1-2002 [73].

As shown in Fig. 16, since the die-sinking micro-EDM and micro-EDM drilling methods are thermal methods, the surfaces have higher SR, as also seen in the SEM views (Figs. 12 and 13) due to melting and re-solidification of the material during the drilling process. Since orbital drilling and conventional drilling methods are mechanical, the surfaces obtained in these processes are smoother than die-sinking micro-EDM and micro-EDM drilling methods. The increase in SR values in thermal machining processes is a result of the fact that the chips removed by melting from the surface adhere to the surface again, forming a rough machined surface in these processes [74–76]. When the samples wrought and WAAM samples are compared, die-sinking micro-EDM and micro-EDM drilling methods caused higher R_a values in the WAAM-fabricated sample due to the high hardness and high dislocation density of this sample. In contrast, orbital drilling and conventional drilling methods, based on mechanical chip removal, resulted in lower SR of the WAAM sample compared to the wrought material. When all drilling methods used in this study were compared, the SR of the holes obtained with orbital and conventional drilling methods varied depending on the evacuation of removed chips. In these methods, the removed chip particles are evacuated from the helixes on the end mill and the drill, which serve for chip evacuation, respectively. Generally, the SR value generated in conventional drilling was lower than in orbital drilling, since the drill cutting form and helix angle improve chip evacuation, as shown in Fig. 16. R_a values obtained in die-sinking micro-EDM and micro-EDM drilling methods varied depending on the evacuation of the molten debris. However, in general, R_a roughness values were higher in die-sinking method than micro-EDM drilling method. Similarly, the average maximum roughness depth R_{max} values were higher in the micro-EDM drilling method than in the die-sinking method, since sparking, that is, local breaking off from the surface of the workpiece, is more in the micro-EDM drilling method. By obtaining the SR within the range of appropriate values, the fatigue-fracture strengths and corrosion resistance of the material increase as well as an aesthetically good appearance on the surface can be achieved [77].

The measurement locations and values of microhardness tests across the cross-sections of all test specimens drilled by thermal and mechanical drilling methods are shown in Figs. 17 and 18.

As discussed earlier, the formation of a recast layer on the surface of the samples drilled with die-sinking micro-EDM and micro-EDM drilling methods was shown in detail in SEM and EDS analyses. In thermal methods, the recast layer has higher hardness values than the substrate material due to rapid cooling due to direct contact of the molten

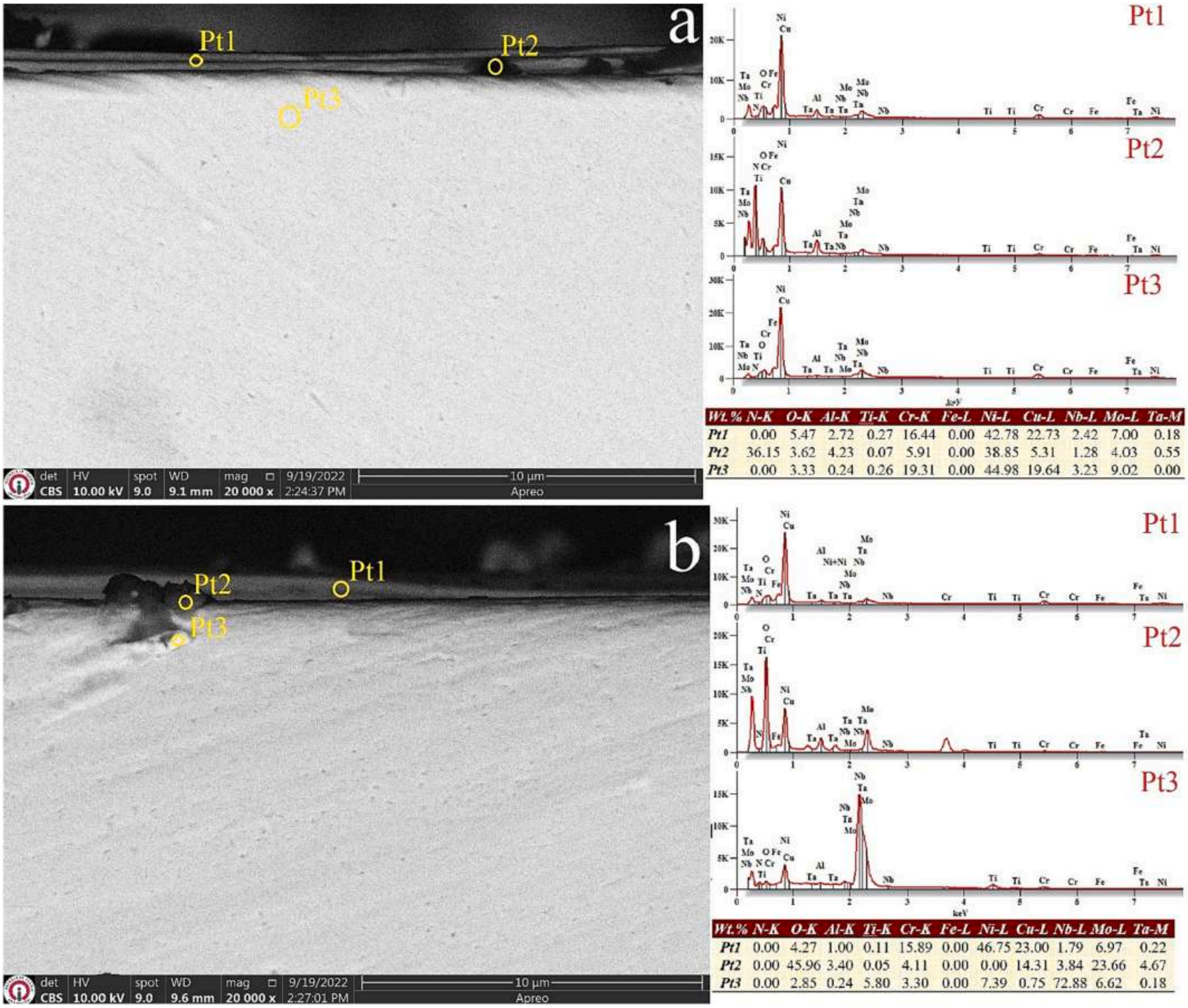

Wt.%	N-K	O-K	Al-K	Ti-K	Cr-K	Fe-L	Ni-L	Cu-L	Nb-L	Mo-L	Ta-M
Pt1	0.00	5.47	2.72	0.27	16.44	0.00	42.78	22.73	2.42	7.00	0.18
Pt2	36.15	3.62	4.23	0.07	5.91	0.00	38.85	5.31	1.28	4.03	0.55
Pt3	0.00	3.33	0.24	0.26	19.31	0.00	44.98	19.64	3.23	9.02	0.00

Wt.%	N-K	O-K	Al-K	Ti-K	Cr-K	Fe-L	Ni-L	Cu-L	Nb-L	Mo-L	Ta-M
Pt1	0.00	4.27	1.00	0.11	15.89	0.00	46.75	23.00	1.79	6.97	0.22
Pt2	0.00	45.96	3.40	0.05	4.11	0.00	0.00	14.31	3.84	23.66	4.67
Pt3	0.00	2.85	0.24	5.80	3.30	0.00	7.39	0.75	72.88	6.62	0.18

Fig. 14. Recast layer formation in the orbital drilling process: (a) wrought and (b) additively manufactured specimen.

material with the water during drilling. For example, in the die-sinking micro-EDM method, the hardness value of the recast layer was determined as 570 HV and 552 HV for wrought and WAAMs. In comparison, these values were determined as 628 HV and 635, respectively, for micro-EDM drilling. This results from instantaneous sparking and heat input and then the rapid cooling that occurs in thermal methods as a result of spraying pure pressurized water from inside the electrode tube and outside the electrode with spiral hoses.

On the other hand, in mechanical drilling methods, drilling is applied with the effect of mechanical cutting forces without causing any melting in the sample. Therefore, no recast layer was formed in the samples drilled with these methods. However, as seen in the cross-sectional surface hardness indentations of the drilled region, it was observed that the hardness values reached approximately twice the hardness values of the substrate material due to the strain hardening effect of the mechanical cutting forces in the regions 5–15 μm away from the surface. Rajguru and Vasudevan [45] suggested that Inconel 625 alloy has a high tendency to hard layer formation on machined surfaces during the end milling operation. In this context, it has also been reported that the region affected by machining, where the hardness increases, is in the range of 70 μm to 80 μm from the surface, and the machined surface exhibits a higher hardness than the base material due to the strain hardening caused by machining.

It can be summarized that in the cross sections of the holes obtained in both wrought and WAAMs with four different drilling methods, the microhardness value changes in the region, which is approximately 5–35 μm in depth from the surface. In other words, it has been determined that the hardness of the machined surface reaches a higher value than the base material due to thermal effects and/or strain hardening as it approaches the machining surface. Drilling with thermal methods caused a lower increase in hardness values than with mechanical drilling methods. This situation can be attributed to the fact that the recast layer is brittle because it is an oxide layer.

4. Conclusions

In this study, the orbital and conventional drilling methods, which are widely used in the production of precision holes in mass production, and die-sinking micro-EDM and micro-EDM drilling methods, which are used for drilling parts where hard cutting tools such as drills and milling have difficulty in drilling, were investigated to perforate the wrought and WAAMed Inconel 625 samples. The effect on the drillability of the

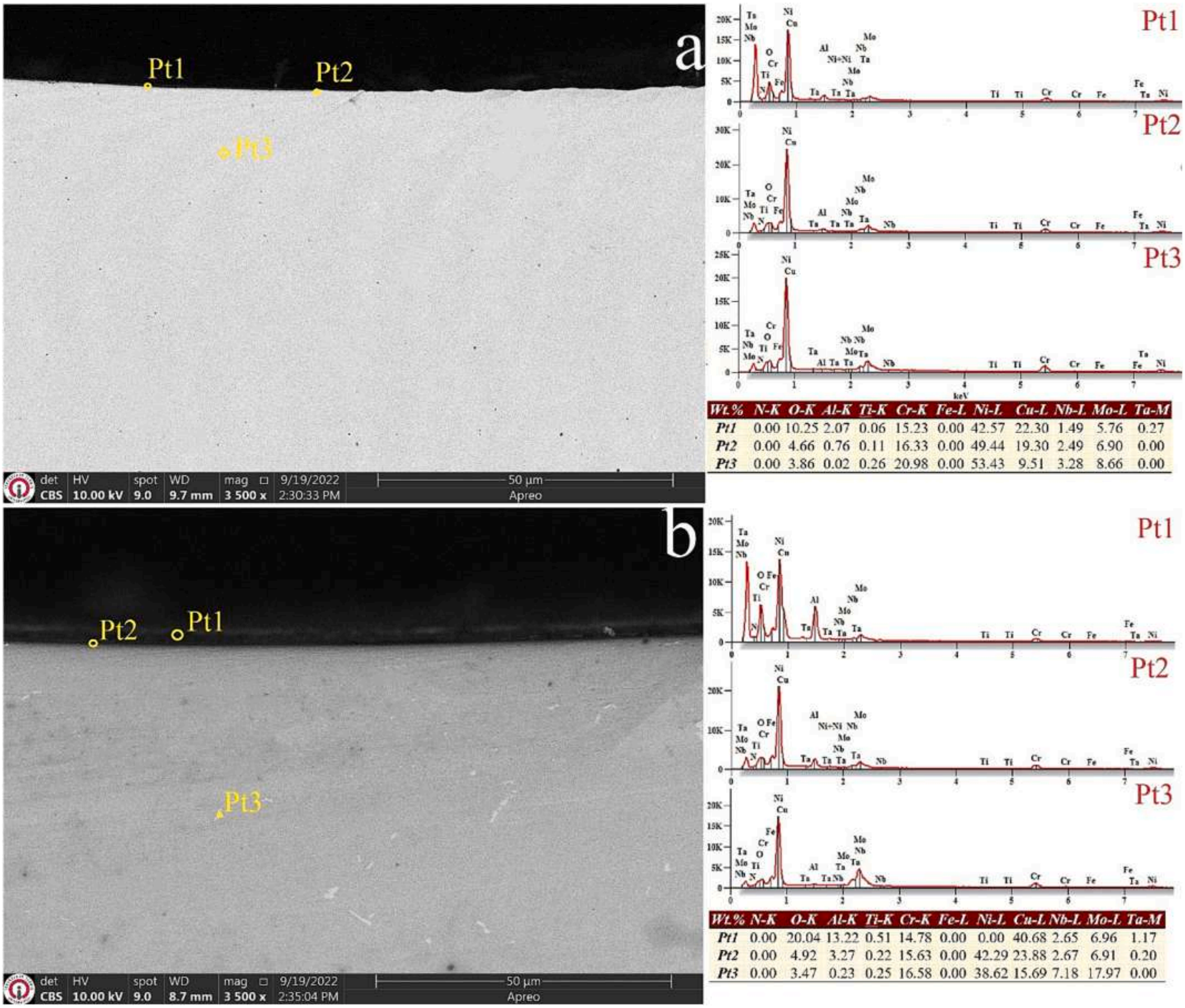

Wt.%	N-K	O-K	Al-K	Ti-K	Cr-K	Fe-L	Ni-L	Cu-L	Nb-L	Mo-L	Ta-M
Pt1	0.00	10.25	2.07	0.06	15.23	0.00	42.57	22.30	1.49	5.76	0.27
Pt2	0.00	4.66	0.76	0.11	16.33	0.00	49.44	19.30	2.49	6.90	0.00
Pt3	0.00	3.86	0.02	0.26	20.98	0.00	53.43	9.51	3.28	8.66	0.00

Wt.%	N-K	O-K	Al-K	Ti-K	Cr-K	Fe-L	Ni-L	Cu-L	Nb-L	Mo-L	Ta-M
Pt1	0.00	20.04	13.22	0.51	14.78	0.00	0.00	40.68	2.65	6.96	1.17
Pt2	0.00	4.92	3.27	0.22	15.63	0.00	42.29	23.88	2.67	6.91	0.20
Pt3	0.00	3.47	0.23	0.25	16.58	0.00	38.62	15.69	7.18	17.97	0.00

Fig. 15. Recast layer formation in the conventional drilling method: (a) wrought and (b) additively manufactured sample.

parts is presented as a comparative study. The obtained results are briefly summarized as follows:

1- The mechanical (hardness, residual stress) and characteristic properties (grain size, XRD orientation) of Inconel 625 alloys produced by forging and WAAM have a great influence on the dimensional accuracy, surface roughness, microhardness, and surface integrity of the holes obtained by thermal drilling and conventional drilling methods.
2- It has been determined that the hole entrance diameters obtained in the workpieces are larger than the hole exit diameters due to the wear of the electrode and cutting tool used in all drilling methods.
3- The difference between hole inlet and outlet diameters was greater in the WAAM Inconel 625 alloy than the wrought one due to the less homogeneity (microstructure and hardness), high residual stress, and high dislocation density. This caused the hole kerf angle obtained in WAAM specimens to be larger than that of the wrought alloy.
4- Kerf results showed that the samples produced by WAAM caused more wear on the cutting tool than the wrought Inconel samples due to their higher hardness value.
5- While the re-cast layer (white layer) is detected on the inner walls of the holes drilled with die-sinking micro-EDM and micro-EDM drilling methods, which are drilling methods based on the thermal principle; no white layer was observed in the methods which are based on mechanical chip removal, namely orbital and conventional drilling. In die-sinking micro-EDM, the white layer was 25 μm and 20 μm thick in WAAM and wrought samples, respectively, while these values increased to 50 μm and 35 μm in micro-EDM drilling, respectively.
6- Since wrought Inconel alloy with lower hardness can be drilled more easily in thermal processes, molten residues (debris) that break off during drilling are less adhered to the surface. This resulted in a lower amount of re-cast layer (white layer) on the surfaces of the processed wrought alloy compared to WAAM.
7- According to the results of all experiments, the best surface condition in terms of SR was obtained in the order of conventional, orbital, die-sinking, and micro-EDM drilling methods.
8- In mechanical machining, WAAM samples show higher surface quality due to their high hardness, while in thermal processing methods, the surface quality of the wrought material is better due to its more homogeneous structure (less residual stress and dislocation

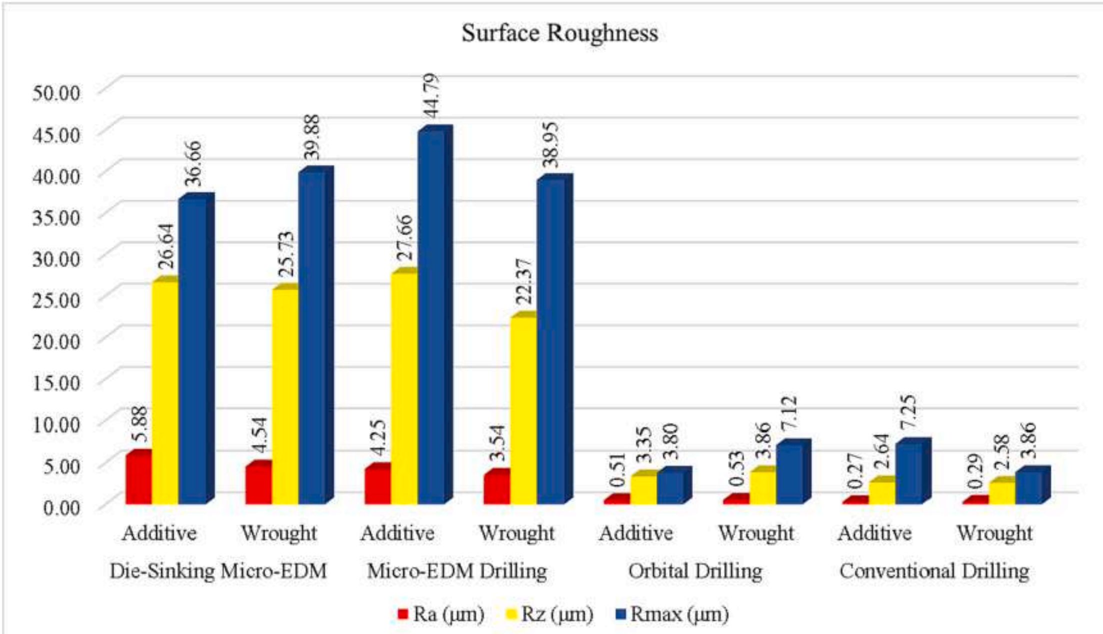

Fig. 16. Comparison of SR values of both wrought and WAAM-produced Inconel 625 alloy specimens drilled by die-sinking micro-EDM, micro-EDM drilling, orbital, and conventional drilling methods.

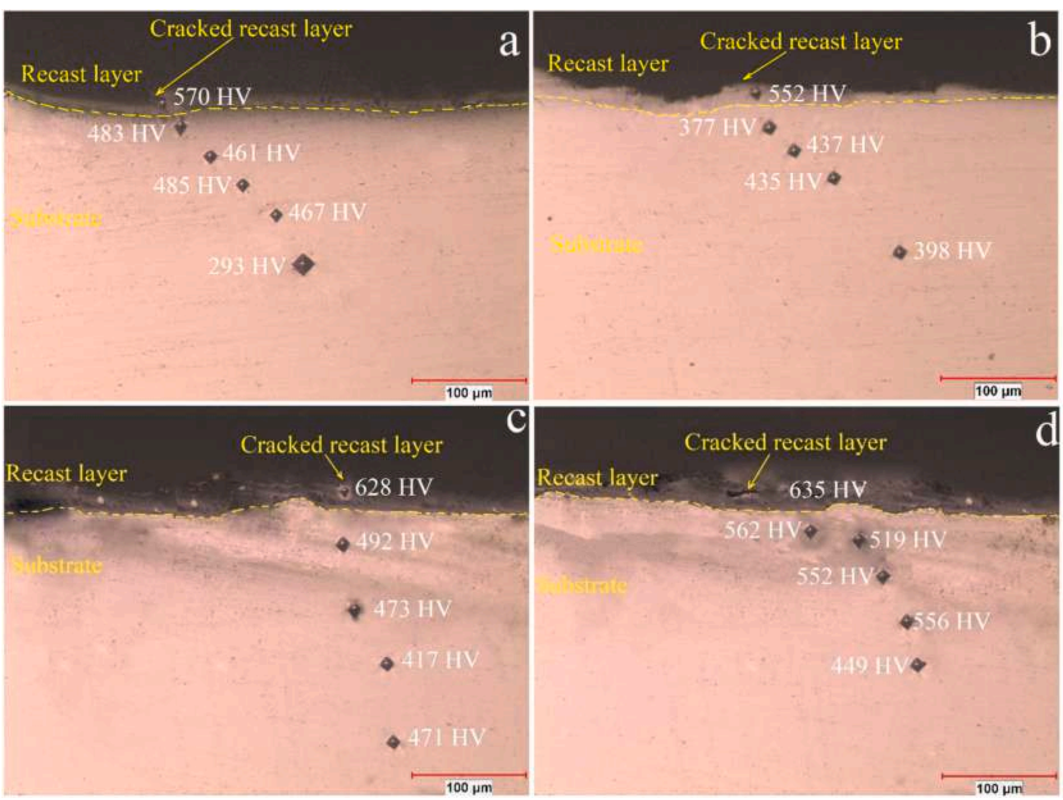

Fig. 17. Microhardness indentations across the cross-sectional surfaces of the samples drilled by thermal drilling methods from the surface to inner sections: a) Die-sinking micro-EDM of wrought specimen, b) Die-sinking micro-EDM of WAAM sample, c) micro-EDM drilling of wrought sğecimen, and d) micro-EDM drilling of WAAM sample.

density).

It was determined that the microhardness value increased from the surface to a depth of 25 μm in the regions processed by thermal and mechanical drilling methods. However, the increase in hardness values obtained in mechanical methods is higher than in thermal methods. This is due to the fact that strain hardening occurs on the surface in mechanical processing, whereas the recast layer formed by thermal methods is more fragile because it is oxide-based and formed as a result of a rapid heating-cooling cycle.

The results showed that orbital and conventional drilling methods

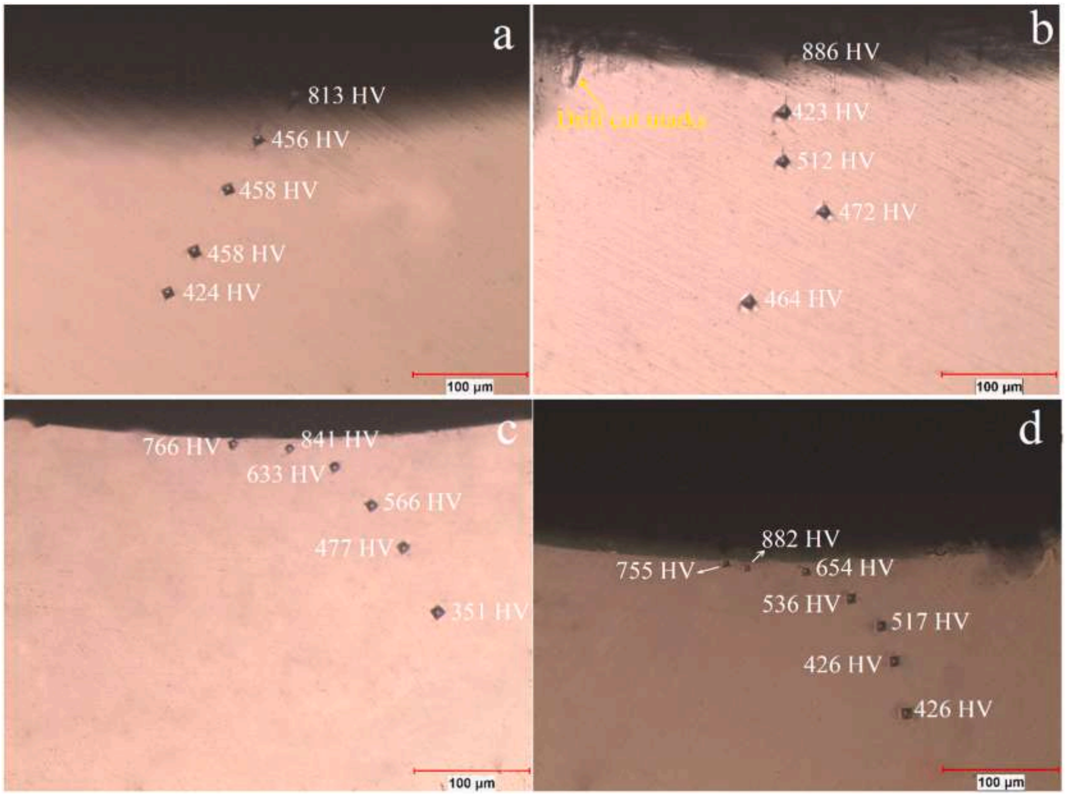

Fig. 18. Microhardness indentations across the cross-sectional surfaces of the samples drilled by mechanical drilling methods from the surface to inner sections: a) orbital drilling of wrought specimen, b) orbital drilling of WAAM sample, c) conventional drilling of wrought specimen, and d) conventional drilling of WAAM sample.

will be more advantageous than die-sinking micro-EDM and micro-EDM drilling methods in areas where dimensional accuracy is very important such as in the aerospace industry. Because in the holes obtained by using end mill and drill bit, the inlet and outlet dimensions are closer to the desired hole diameter and kerf formation is almost non-existent. On the other hand, die-sinking micro-EDM and micro-EDM drilling methods can be used to remove tools such as reamer, drill, bolt, which are difficult to remove due to the fact that they are often broken in the workpiece for repair purposes in the industry since they give results close to orbital and conventional drilling methods.

Nomenclature and abbreviations

ANOVA	analysis of variance
AM	additive manufacturing
ASTM	The American Society for Testing and Materials
CAD	computer aided design
CNC	Computerized Numerical Control
D	crystal grain size (nm)
EDM	electrical discharge machining
EDS	energy dispersive spectroscopy
EWR	electrode wear rate
Feed rate	(mm/min)
MAM	metal additive manufacturing
MFA EDM	magnetic-field-assisted electrical discharge machining
MRR	material removal rate (mm^3/min)
P	density (g/cm^3)
Peck depth	mm/rev
ROC	radial overcut
rpm	revolutions per minute
SCD	surface crack density
SEM	scanning electron microscope
Spindle speed	rpm
SR	surface roughness
XRD	X-ray diffraction
XRF	X-ray fluorescence
WAAM	wire arc additive manufacturing
WEDM	wire electrical discharge machining
WLT	white layer thickness
ε	microstrain
δ	dislocation density (nm^{-2})

Declaration of competing interest

The authors declare that they have no known competing financial interests or personal relationships that could have appeared to influence the work reported in this paper.

Acknowledgements

The authors thank Mr. Batuhan Turgut and the R&D Center of the Gedik Welding, Istanbul-Türkiye, for their technical support while manufacturing the WAAM component. They are also grateful to the personnel of the Molding Department of Haier Europe, Candy-Hoover, Eskişehir-Türkiye, for their technical support in the drilling processes performed on the Oscarmax SD400 EDM, Makino S33 model CNC, Furkan brand EDM machines, and to Technical Teacher Yasin ÖZEN, who is the technical manager of the Mechanical Test Laboratory of MEGEM (Vocational Training and Development Center), Eskişehir-Türkiye, for his support in obtaining microscope images.

References

[1] Reed RC. The superalloys: fundamentals and applications. Cambridge, U.K.: Cambridge University Press; 2008.
[2] Satish GJ, Gaitonde VN, Kulkarni VN. Traditional and non-traditional machining of nickel-based superalloys: a brief review. Mater Today: Proc 2021;44:1448–54. https://doi.org/10.1016/j.matpr.2020.11.632.
[3] Khanna N, Zadafiya K, Patel T, Kaynak Y, Rashid RAR, Vafadar A. Review on machining of additively manufactured nickel and titanium alloys. J Mater Res Technol 2021;15:3192–221. https://doi.org/10.1016/j.jmrt.2021.09.088.
[4] Korkmaz ME, Gupta MK, Boy M, Yaşar N, Krolczyk GM, Günay M. Influence of duplex jets MQL and nano-MQL cooling system on machining performance of nimonic 80A. J Manuf Process 2021;69:112–24. https://doi.org/10.1016/j.jmapro.2021.07.039.
[5] Pinheiro C, Kondo MY, Amaral SS, Callisaya ES, De Souza JVC, De Sampaio Alves MC, Ribeiro MV. Effect of machining parameters on turning process of inconel 718. Mater Manuf Process 2021;36(12):1421–37. https://doi.org/10.1080/10426914.2021.1914839.
[6] Toyserkani E, Sarker D, Ibhadode OO, Liravi F, Russo P, Taherkhani K. Metal additive manufacturing. 2021.
[7] Kannan GB, Rajendran DK. A review on status of research in metal additive manufacturing. In: Wimpenny D, Pandey P, Kumar L, editors. Advances in 3D printing & additive manufacturing technologies. Singapore: Springer; 2017. p. 95–100. https://doi.org/10.1007/978-981-10-0812-2_8.
[8] Ikeo N, Fukuda H, Matsugaki A, Inoue T, Serizawa A, Matsuzaka T, Ishimoto T, Ozasa R, Gokcekaya O, Nakano T. 3D puzzle in cube pattern for Anisotropic/Isotropic mechanical control of structure fabricated by metal additive manufacturing. Crystals 2021;11:959. https://doi.org/10.3390/cryst11080959.
[9] Korkmaz ME, Gupta MK, Robak G, Moj K, Krolczyk GM, Kuntoğlu M. Development of lattice structure with selective laser melting process: a state of the art on properties, future trends and challenges. J Manuf Process 2022;81:1040–63. https://doi.org/10.1016/j.jmapro.2022.07.051.
[10] Tofail SA, Koumoulos EP, Bandyopadhyay A, Bose S, O'Donoghue L, Charitidis C. Additive manufacturing: scientific and technological challenges, market uptake and opportunities. Mater Today 2018;21(1):22–37. https://doi.org/10.1016/j.mattod.2017.07.001.
[11] Gebhardt A, Hötter JS. Additive manufacturing: 3D printing for prototyping and manufacturing. Munich, Germany: Carl Hanser Verlag GmbH & Company KG; 2016.
[12] Derekar KS. A review of wire arc additive manufacturing and advances in wire arc additive manufacturing of aluminium. Mater Sci Technol 2018;34(8):895–916. https://doi.org/10.1080/02670836.2018.1455012.
[13] Liu J, Xu Y, Ge Y, Hou Z, Chen S. Wire and arc additive manufacturing of metal components: a review of recent research developments. Int J Adv Manuf Technol 2020;111:149–98. https://doi.org/10.1007/s00170-020-05966-8.
[14] Jin W, Zhang C, Jin S, Tian Y, Wellmann D, Liu W. Wire arc additive manufacturing of stainless steels: a review. Appl Sci 2020;10(5):1563. https://doi.org/10.3390/app10051563.
[15] Lui EW, Medvedev AE, Edwards D, Qian M, Leary M, Brandt M. Microstructure modification of additive manufactured ti-6Al-4V plates for improved ballistic performance properties. J Mater Process Technol 2022;301:117436. https://doi.org/10.1016/j.jmatprotec.2021.117436.
[16] Chen X, Shang X, Zhou Z, Chen SG. A review of the development status of wire arc additive manufacturing technology. Adv Mater Sci Eng 2022;1–28. https://doi.org/10.1155/2022/5757484.
[17] Günen A, Gürol U, Koçak M, Çam G. Investigation into the influence of boronizing on the wear behavior of additively manufactured inconel 625 alloy at elevated temperature. Prog Addit Manuf 2023;1–21. https://doi.org/10.1007/s40964-023-00398-8.
[18] Ahsan MR, Seo GJ, Fan X, Liaw PK, Motaman S, Haase C, Kim DB. Effects of process parameters on bead shape, microstructure, and mechanical properties in wire+ arc additive manufacturing of Al0.1CoCrFeNi high-entropy alloy. J Manuf Process 2021;68:1314–27. https://doi.org/10.1016/j.jmapro.2021.06.047.
[19] Gokcekaya O, Ishimoto T, Hibino S, Yasutomi J, Narushima T, Nakano T. Unique crystallographic texture formation in inconel 718 by laser powder bed fusion and its effect on mechanical anisotropy. Acta Mater 2021;212:116876. https://doi.org/10.1016/j.actamat.2021.116876.
[20] Wu Y, Li C, Xia X, Liang H, Qi Q, Liu Y. Precipitate coarsening and its effects on the hot deformation behavior of the recently developed γ'-strengthened superalloys. J Mater Sci Technol 2021;67:95–104. https://doi.org/10.1016/j.jmst.2020.06.025.
[21] Hu Y, Lin X, Li Y, Ou Y, Gao X, Zhang Q, Huang W. Microstructural evolution and anisotropic mechanical properties of inconel 625 superalloy fabricated by directed energy deposition. J Alloys Compd 2021;870:159426. https://doi.org/10.1016/j.jallcom.2021.159426.
[22] Luo J, Yu W, Xi C, Zhang C, Ma C. Preparation of ultrafine-grained GH4169 superalloy by high-pressure torsion and analysis of grain refinement mechanism. J Alloys Compd 2019;777:157–64. https://doi.org/10.1016/j.jallcom.2018.10.385.
[23] Cam G, Fischer A, Ratjen R, dos Santos JF, Kocak M. Properties of Laser Beam Welded Superalloys Inconel 625 and 718. In: Mordike BL, editor. Proc. of 7th European Conference on Laser Treatment of Materials, ECLAT ;98, September 21-23, 1998, Hannover, Germany. Frankfurt: Werkstoff-Informationsgeselschaft mbH; 1998. p. 333–8.
[24] Shahwaz M, Nath P, Sen I. A critical review on the microstructure and mechanical properties correlation of additively manufactured nickel-based superalloys. J Alloys Compd 2022;164530. https://doi.org/10.1016/j.jallcom.2022.164530.
[25] Sarıkaya M, Gupta MK, Tomaz I, Pimenov DY, Kuntoğlu M, Khanna N, Krolczyk GM. A state-of-the-art review on tool wear and surface integrity characteristics in machining of superalloys. CIRP J Manuf Sci Technol 2021;35:624–58. https://doi.org/10.1016/j.cirpj.2021.08.005.
[26] Pusavec F, Deshpande A, Yang S, M'Saoubi R, Kopac J, Dillon Jr OW, et al. Sustainable machining of high temperature nickel alloy–Inconel 718: part 1–predictive performance models. J Clean Prod 2014;81:255–69. https://doi.org/10.1016/j.jclepro.2014.06.040.
[27] Karatas MA, Gokkaya H. A review on machinability of carbon fiber reinforced polymer (CFRP) and glass fiber reinforced polymer (GFRP) composite materials. Def Technol 2018;14(4):318–26. https://doi.org/10.1016/j.dt.2018.02.001.
[28] Tanjilul M, Ahmed A, Kumar AS, Rahman M. A study on EDM debris particle size and flushing mechanism for efficient debris removal in EDM-drilling of inconel 718. J Mater Process Technol 2018;255:263–74. https://doi.org/10.1016/j.jmatprotec.2017.12.016.
[29] Ross NS, Srinivasan N, Amutha P, Gupta MK, Korkmaz ME. Thermo-physical, tribological and machining characteristics of hastelloy C276 under sustainable cooling/lubrication conditions. J Manuf Process 2022;80:397–413. https://doi.org/10.1016/j.jmapro.2022.06.018.
[30] Khanna N, Agrawal C, Pimenov DY, Singla AK, Machado AR, da Silva LRR, Krolczyk GM. Review on design and development of cryogenic machining setups for heat resistant alloys and composites. J Manuf Process 2021;68:398–422. https://doi.org/10.1016/j.jmapro.2021.05.053.
[31] Sharma S, Vates UK, Bansal A. Influence of die-sinking EDM parameters on machining characteristics of alloy 625 and alloy 718: a comparative analysis. Mater Today: Proc 2022;50:2493–9. https://doi.org/10.1016/j.matpr.2021.10.450.
[32] Singh P, Yadava V, Narayan A. Micro-EDM performance of inconel 718 superalloy with and without ultrasonic vibration. Int J Precis Technol 2019;8(2–4):174–89. https://doi.org/10.1504/IJPTECH.2019.100949.
[33] Wang C, Zhao J, Zhou Y. Mechanics and dynamics study of helical milling process for nickel-based superalloy. Int J Adv Manuf Technol 2020;106(5):2305–16. https://doi.org/10.1007/s00170-019-04793-w.
[34] Vasudevan B, Natarajan Y, Sivalingam V, Krolczyk G, Tandon P. Insights into drilling film cooling holes on ceramic-coated nickel-based superalloys. Arch Civ Mech Eng 2022;22(3):1–30. https://doi.org/10.1007/s43452-022-00465-x.
[35] Mishra DK, Rahul, Datta S, Masanta M, Mahapatra SS. Through hole making by electro-discharge machining on Inconel 625 super alloy using hollow copper tool electrode. Proc. Inst. Mech. Eng. E 2019;233(2):348–70. https://doi.org/10.1177/0954408918784701.
[36] Ahmed A, Tanjilul M, Rahman M, Kumar AS. Ultrafast drilling of inconel 718 using hybrid EDM with different electrode materials. Int J Adv Manuf Technol 2020;106(5):2281–94. https://doi.org/10.1007/s00170-019-04769-w.
[37] Venkatesan K, Nagendra KU, Anudeep CM, Cotton AE. Experimental investigation and parametric optimization on hole quality assessment during micro-drilling of inconel 625 superalloy. Arabian J Sci Eng 2021;46(3):2283–309. https://doi.org/10.1007/s13369-020-04992-8.
[38] Attanasio A. Micro drilling of hard-to-cut materials: an experimental analysis. Int J Mechatron Manuf Syst 2017;10(4):299–320. https://doi.org/10.1504/IJMMS.2017.088927.
[39] Liu E, An W, Xu Z, Zhang H. Experimental study of cutting-parameter and tool life reliability optimization in inconel 625 machining based on wear map approach. J Manuf Process 2020;53:34–42. https://doi.org/10.1016/j.jmapro.2020.02.006.
[40] Chen Z, Huang C, Li B, Jiang G, Tang Z, Niu J, Liu H. Experimental study on surface integrity of inconel 690 milled by coated carbide inserts. Int J Adv Manuf Technol 2022;1–18. https://doi.org/10.1007/s00170-022-09456-x.
[41] Liao ZR, la Monaca A, Murray J, Speidel A, Ushmaev D, Clare A, Axinte D, M'Saoubi R. Surface integrity in metal machining - part I: fundamentals of surface characteristics and formation mechanisms. Int J Mach Tool Manuf 2021;162:103687. https://doi.org/10.1016/j.ijmac htools.2020.103687.
[42] Behera A, Behera A. In: Superalloys. Advanced materials: an introduction to modern materials science; 2022. p. 225–61. https://doi.org/10.1007/978-3-030-80359-9.
[43] Jayakumar K. Optimization of process parameters during EDM on inconel alloy 625. Trends Manuf Eng Manag 2021:897–904. https://doi.org/10.1007/978-981-15-4745-4_77.
[44] Rajguru R, Vasudevan H. Investigating the effect of cutting conditions and tool geometry on surface roughness in dry end milling of inconel 625 using TiAlSiN ultra hard coated solid carbide tool. Adv Mater Process Technol 2020;1–10. https://doi.org/10.1080/2374068X.2020.1855964.
[45] Rajguru RR, Vasudevan H. A study of micro hardness in the machining of inconel 625 using TiAlSiN coated tools under dry cutting conditions. Adv Mater Process Technol 2022;1–11. https://doi.org/10.1080/2374068X.2022.2100035.
[46] Khan MY, Rao PS, Pabla BS. An experimental study on magnetic field-assisted-EDM process for Inconel-625. Adv Mater Process Technol 2022;1–27. https://doi.org/10.1080/2374068X.2022.2036450.
[47] Imran M, Mativenga PT, Gholinia A, Withers PJ. Comparison of tool wear mechanisms and surface integrity for dry and wet micro-drilling of nickel-base superalloys. Int J Mach Tool Manuf 2014;76:49–60. https://doi.org/10.1016/j.jmac htools.2013.10.002.
[48] Wang Y, Chen X, Shen Q, Su C, Zhang Y, Jayalakshmi S, Singh RA. Effect of magnetic field on the microstructure and mechanical properties of inconel 625

superalloy fabricated by wire arc additive manufacturing. J Manuf Process 2021; 64:10–9. https://doi.org/10.1016/j.jmapro.2021.01.008.
[49] Boukhoubza I, Khenfouch M, Achehboune M, Mothudi BM, Zorkani I, Jorio A. X-ray diffraction investigations of nanostructured ZnO coated with reduced graphene oxide. J Phys Conf Ser 2019;1292(1):012011. https://doi.org/10.1088/1742-6596/1292/1/012011.
[50] Bindu P, Thomas S. Estimation of lattice strain in ZnO nanoparticles: X-ray peak profile analysis. J Theoret Appl Phys 2014;8(4):123–34. https://doi.org/10.1007/s40094-014-0141-9.
[51] Patterson AL. The scherrer formula for X-ray particle size determination. Phys Rev 1939;56(10):978. https://doi.org/10.1103/PhysRev.56.978.
[52] Sanchez JA, Cabanes I, Lopez de Lacalle LN, Lamikiz A. Development of optimum electrodischarge machining technology for advanced ceramics. Int J Adv Manuf Technol 2001;18(12):897–905. https://doi.org/10.1007/PL00003958.
[53] Davim JP, editor. Modern machining technology: a practical guide. Elsevier; 2011. ISBN 978-0-85709-099-7.
[54] Davim JP. Nontraditional machining processes, manufacturing process selection handbook. In: London, U.K: Springer; 2013. p. 205–26. https://doi.org/10.1007/978-1-4471-5179-1.
[55] Davim JP, editor. Machining: fundamentals and recent advances; 2008. https://doi.org/10.1007/978-1-84800-213-5.
[56] Baral SK, Pallavi P, Utkarshaa A. Effect of nichroloy coated electrode on machining performance of electrical discharge machining using inconel 625. Mater Today Proc 2021;45:7894–900. https://doi.org/10.1016/j.matpr.2020.12.615.
[57] Ceritbinmez F, Özkan V, Saracoglu G, Yapici A. MWCNTs doped GFRPs drilling: crosscheck among holes obtained by alternative manufacturing methods. Int J Adv Manuf Technol 2022;118(1):33–41. https://doi.org/10.1007/s00170-021-07181-5.
[58] Tandekar N, Sandeep A, Kumar P, Miryalkar P, Valleti K. An assessment of tool life in drilling of inconel 718 using cathodic arc PVD coated carbide bits. Int J Adv Manuf Technol 2022;120(7):4821–33. https://doi.org/10.1007/s00170-022-09057-8.
[59] Khanna N, Agrawal C, Gupta MK, Song Q. Tool wear and hole quality evaluation in cryogenic Drilling of Inconel 718 superalloy. Tribol Int 2020;143:106084. https://doi.org/10.1016/j.triboint.2019.106084.
[60] Skrabalak G. Influence of electrode tool length on the micro EDM drilling performance. Procedia CIRP 2018;68:594–8. https://doi.org/10.1016/j.procir.2017.12.120.
[61] Yangfan W, Xizhang C, Chuanchu S. Microstructure and mechanical properties of inconel 625 fabricated by wire-arc additive manufacturing. Surf Coat Technol 2019;374:116–23. https://doi.org/10.1016/j.surfcoat.2019.05.079.
[62] Charpagne MA, Hestroffer JM, Polonsky AT, Echlin MP, Texier D, Valle V, Stinville JC. Slip localization in inconel 718: a three-dimensional and statistical perspective. Acta Mater 2021;215:117037. https://doi.org/10.1016/j.actamat.2021.117037.
[63] Pellicer N, Ciurana J, Delgado J. Tool electrode geometry and process parameters influence on different feature geometry and surface quality in electrical discharge machining of AISI H13 steel. J Intell Manuf 2011;22(4):575–84. https://doi.org/10.1007/s10845-009-0320-8.
[64] Kivak T, Habali K, Şeker U. The effect of cutting paramaters on the hole quality and tool wear during the drilling of inconel 718. Gazi University J Sci 2012;25(2):533–40.
[65] Zhu D, Zhang X, Ding H. Tool wear characteristics in machining of nickel-based superalloys. Int J Mach Tool Manuf 2013;64:60–77. https://doi.org/10.1016/j.ijmachtools.2012.08.001.
[66] Ni H, Gong H, Dong YH, Fang FZ, Wang Y. A comparative investigation on hybrid EDM for drilling small deep holes. Int J Adv Manuf Technol 2018;95(1):1465–72. https://doi.org/10.1007/s00170-017-1282-1.
[67] Pham DT, Dimov SS, Bigot S, Ivanov A, Popov K. Micro-EDM—recent developments and research issues. J Mater Process Technol 2004;149(1–3):50–7. https://doi.org/10.1016/j.jmatprotec.2004.02.008.
[68] Ji R, Liu Y, Diao R, Xu C, Li X, Cai B, Zhang Y. Influence of electrical resistivity and machining parameters on electrical discharge machining performance of engineering ceramics. PLoS One 2014;9(11):e110775. https://doi.org/10.1371/journal.pone.0110775.
[69] Malik NS, Bharti PS. Multi-objective parametric optimization during micro-EDM drilling of ti-6Al-4V using teaching learning based optimization algorithm. Mater Today Proc 2022;62(1). https://doi.org/10.1016/j.matpr.2022.03.257.
[70] Moore MA. The relationship between the abrasive wear resistance, hardness and microstructure of ferritic materials. Wear 1974;28(1):59–68. https://doi.org/10.1016/0043-1648(74)90101-X.
[71] Misra A, Finnie I. A review of the abrasive wear of metals. J Eng Mater Technol 1982;104(2):94–101. https://doi.org/10.1115/1.3225058.
[72] Mazhnik E, Oganov AR. A model of hardness and fracture toughness of solids. J Appl Phys 2019;126(12):125109. https://doi.org/10.1063/1.5113622.
[73] American Society of Mechanical Engineers. ASME B46. 1–2002, surface texture (surface roughness, waviness and lay). New York, NY, USA: ASME; 2002.
[74] Günen A, Ceritbinmez F, Patel K, Akhtar MA, Mukherjee S, Kanca E, Karakas MS. WEDM machining of MoNbTaTiZr refractory high entropy alloy. CIRP J Manuf Sci Technol 2022;38:547–59. https://doi.org/10.1016/j.cirpj.2022.05.021.
[75] Benardos PG, Vosniakos GC. Predicting surface roughness in machining: a review. Int J Mach Tool Manuf 2003;43(8):833–44. https://doi.org/10.1016/S0890-6955(03)00059-2.
[76] Shastri RK, Mohanty CP, Dash S, Gopal KMP, Annamalai AR, Jen CP. Reviewing performance measures of the die-sinking electrical discharge machining process: challenges and future scopes. Nanomaterials 2022;12(3):384. https://doi.org/10.3390/nano12030384.
[77] Guo C, Wu Z, Wang X, Zhang J. Comparison in performance by emulsion and SiC nanofluids HS-WEDM multi-cutting process. Int J Adv Manuf Technol 2021;116(9):3315–24. https://doi.org/10.1007/s00170-021-07600-7.